Earth Planet. Sci. Lett. 648 (2024) 119107

Contents lists available at ScienceDirect

Earth and Planetary Science Letters

journal homepage: www.elsevier.com/locate/epsl

Shallow crustal rupture in a major M_W 7.5 earthquake above a deep crustal seismic swarm along the Noto Peninsula in western Japan

Chengli Liu [a,*], Yefei Bai [b,c,*], Thorne Lay [d], Ping He [a], Yangmao Wen [e], Xiaoran Wei [b], Neng Xiong [f], Xiong Xiong [a]

[a] *Hubei Subsurface Multi-Scale Imaging Key Laboratory, School of Geophysics and Geomatics, China University of Geosciences, Wuhan, China*
[b] *Ocean College, Zhejiang University, Zhoushan, Zhejiang, 316021, China*
[c] *Hainan Institute, Zhejiang University, Sanya, Hainan, 572024, China*
[d] *Department of Earth and Planetary Sciences, University of California Santa Cruz, Santa Cruz, CA, USA*
[e] *School of Geodesy and Geomatics, Wuhan University, Wuhan, China*
[f] *Department of Earth, Environmental, and Planetary Sciences, Rice University, Houston, TX, USA*

ARTICLE INFO

Editor: J.P. Avouac

Keywords:
Noto earthquake
Joint inversion
Seismic swarms
Fluid migration
Low rupture velocity
Bilateral rupture

ABSTRACT

A damaging M_W 7.5 earthquake struck the western coast of Japan along the Noto Peninsula on January 1, 2024. The initiation of large shallow earthquakes along the Noto Peninsula, particularly above deeper long-duration patchy seismic swarms, presents an unusual seismic phenomenon that warrants in-depth investigation of their interactions. The 2024 earthquake nucleated with an initial low average rupture velocity of 0.5–1.0 km s^{-1} near the up-dip end of a long-lasting seismic swarm that commenced in November 2020. Analysis of dense seismic, geodetic, and tsunami observations provides good resolution of large shallow slip in the crust below the peninsula and extending offshore to the northeast, revealing a heterogeneous slip distribution characterized by bilateral two-stage rupture expansion during the faulting. Up to 8 m of slip occurred in several patches along ~150 km of the southeastward-dipping thrust fault, which extends to near the seafloor along the northwest side of the peninsula. Up to 5 m of uplift occurred along the peninsula's northwestern coast. Up-dip fluid migration appears to have weakened the shallow fault prior to failure and influenced the initial slow rupture expansion, highlighting the need to monitor the evolution of worldwide swarms.

1.Introduction

Prolonged earthquake sequences lasting from days to years that lack a dominant large magnitude (mainshock) event are called earthquake swarms (Mogi, 1963). Volcanic, rifting and hydrothermal regions of the crust frequently host earthquake swarms (e.g. Kisslinger, 1975; Yamashita, 1999; Vidale et al., 2006; Enescu et al., 2009; Hauksson et al., 2013; De Barros et al., 2020), and swarms also occur along portions of subduction zone plate boundaries adjacent to areas that rupture in major earthquakes (Holtkamp and Brudzinski, 2011; Bedford et al., 2015; Marsan et al., 2023). However, regions that produce swarms are seldom directly associated with large mainshock occurrence. Fluid intrusion is generally invoked to account for distributed fault weakening leading to the onset of a swarm, with aseismic slip and redistribution of stress also influencing swarm evolution (Hainzl, 2004; Lohman and McGuire, 2007; Shelly et al., 2016; Yoshida et al., 2017; Ross and Cochran, 2021; Cebry and McLaskey, 2021). Migration of event locations during swarms provides suggestive evidence of fluid intrusion (e.g. Yukutake et al., 2011; Chen et al., 2012; Shelly et al., 2013; Kosuga, 2014; Okada et al., 2015; Ross et al., 2017; Dublanchet and De Barros, 2021). Widespread anthropogenic triggering of seismicity by wastewater injection (Horton, 2012; Ellsworth, 2013) also provides support for the plausible role of fluids in causing swarm activity.

A long-lasting crustal earthquake swarm located below the northeastern end of the Noto Peninsula, Japan, commenced with a rapid increase in seismicity rate around November 2020 and continues to January 1, 2024 (Fig. 1). >20,000 earthquakes with Japan Meteorological Agency (JMA) magnitudes M_j 1 to 5 have been detected (e.g. Nakajima, 2022; Amezawa et al., 2023; Yoshida et al., 2023a; Kato, 2024). The swarm activity (mingled with the magenta- and orange-colored aftershock sequences for larger events in Fig. 1, A to C) is concentrated in four distinct clusters within a 15 km by 15 km area

---

* Corresponding authors.
E-mail addresses: liuchengli@cug.edu.cn (C. Liu), yfbai@zju.edu.cn (Y. Bai).

https://doi.org/10.1016/j.epsl.2024.119107
Received 25 June 2024; Received in revised form 25 October 2024; Accepted 29 October 2024

spanning depths from 10 to 18 km (Fig. S1) (e.g. Nakajima, 2022; Amezawa et al., 2023; Yoshida et al., 2023a). Focal mechanisms are predominantly 35° to 45° dipping thrust faults with near-horizontal compression axes-oriented NW-SE. Geodetic measurements resolve transient deformation with horizontal inflation and uplift of up to 70 mm in the swarm region (Nishimura et al., 2023). The Noto Peninsula has not had active volcanism for 15 Ma, but does have a high geothermal gradient (>50 K km^{-1}), and high-temperature hot springs are found in faulted regions, possibly due to meteoric waters circulating to high heat production granites beneath low conductivity sediments (Umeda et al., 2009). Swarms have been observed in other regions of paleo-volcanoes and paleo-calderas in Japan (e.g. Okada et al., 2015; Yoshida and Hasegawa, 2018; Matsumoto et al., 2021), possibly deriving fluids from old magma chambers (e.g. Yoshida et al., 2023b).

Prior to, and spatially removed from the swarm, a moment-magnitude M_W (moment magnitude) 6.7 thrust earthquake occurred at the western end of the Noto Peninsula on March 25, 2007 (e.g. Kato et al., 2008; Kurahashi et al., 2008), and low-level seismic activity was distributed along a trend to the northeast (Fig. 1A). A fluid-filled reservoir below the 2007 rupture zone has been inferred from seismic and magnetotelluric observations and may have influenced the shallow coseismic slip distribution (e.g. Yoshimura et al., 2008; Kato et al., 2011). The present-day compressional stress regime in the Noto Peninsula is likely associated with crustal shortening along western Honshu that began in the late Miocene, reactivating steeply dipping graben extensional faults that are buried under sediments (Kato et al., 2008; Ishiyama et al., 2017). The fault ruptured in 2007 appears to extend along the Noto Peninsula to the swarm region to the northeast, possibly as a single structure or along several segments.

The largest events originating during and in close spatial proximity to the swarm, all having thrust faulting mechanisms, have included an M_W 5.1 event on June 19, 2022 (Yoshida et al., 2023a), M_W 6.2 and 5.6 events on May 5, 2023 (Kato, 2024; Yoshida et al., 2023b), and an M_W 7.5 event on January 1, 2024 (Fig. 1). The M_W 6.2 and M_W 7.5 events both have hypocenters within the depth range of the swarm, but their ruptures extend up-dip along southeastward dipping thrust faults extending across the shallow crust, reaching to within a few kilometers of the surface (Kato, 2024). Fluid-flow up-dip from the swarm region on a shallow crustal fault has been invoked as the cause of upward earthquake migration observed for the 2023 event (e.g. Yoshida et al., 2023a, 2023b; Kato, 2024). The major 2024 mainshock event produced extensive destruction and loss of life on the Noto Peninsula (Normile, 2024), and its aftershock zone (cyan events in Fig. 1D and E) is much longer than the swarm dimensions, indicating rupture of a distinct, through-going fault dipping toward the southeast. The aftershocks extend southwest to the vicinity of the 2007 event and northeast offshore of the peninsula. Multiple segments can possibly be defined along this trend, but the seismicity is overall well-represented with a single planar fault.

This is a very rare example of a major mainshock earthquake

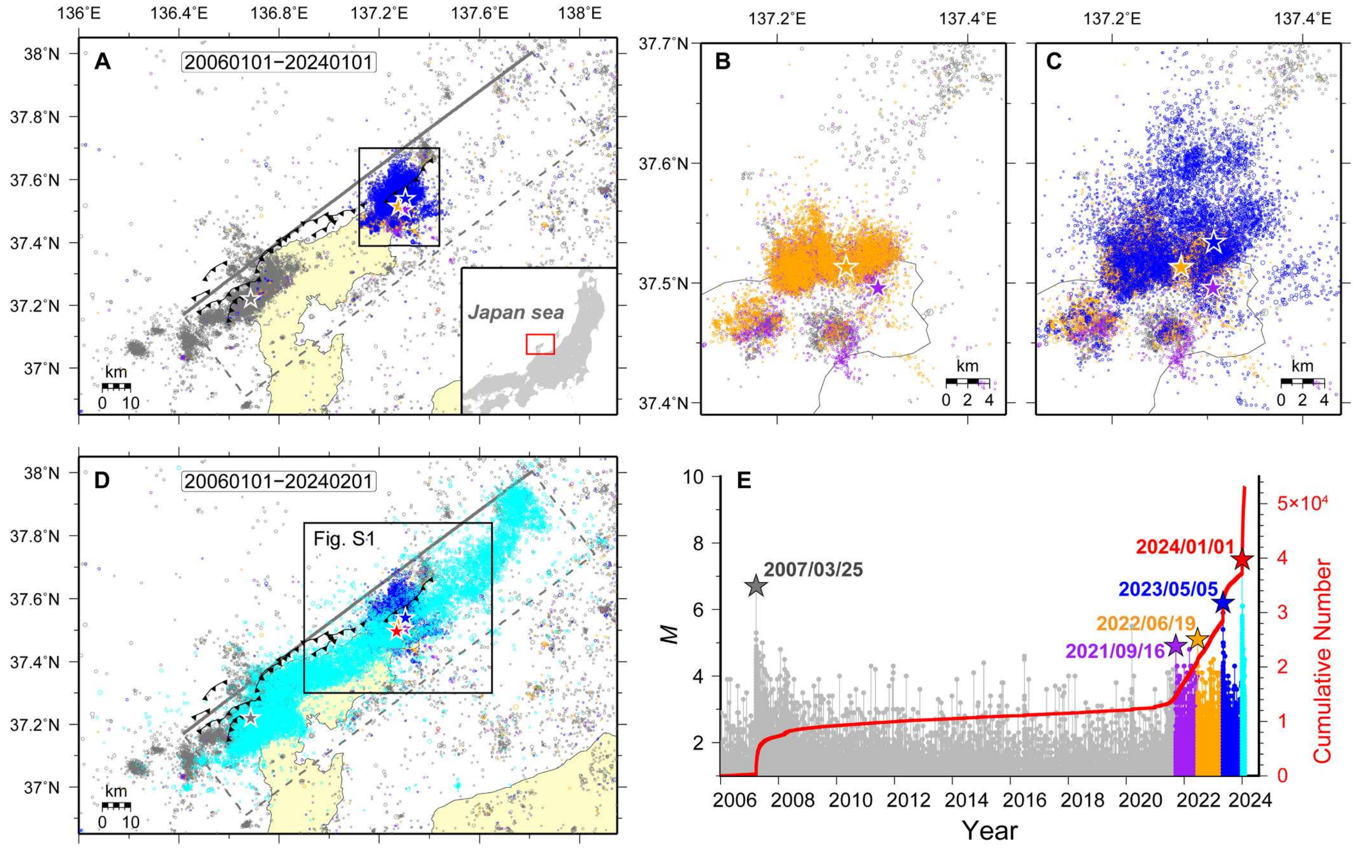

Fig. 1. Seismic activity around the Noto Peninsula from January 1, 2006, to February 1, 2024, from the JMA catalog. (A), Seismic activity with $M_j \geq 1.0$ prior to the January 1, 2024 M_W 7.5 earthquake. Gray circles indicate events before the M_W 4.9 event on September 16, 2021. Color symbols highlight events in varying time intervals during the swarm, some of which are aftershocks of large events in the shallow crust above the swarm region. The black rectangle outlines the Noto swarm region, enlarged in (B) and (C). The gray dashed rectangle indicates the mainshock fault plane used in this study, with the solid line depicting the shallow northwestern edge. B. and C. The swarm activity that occurred in 2021, 2022, and 2023, highlighted by the magenta, orange, and blue-colored circles, respectively, with stars representing the larger events during the seismic swarm. (D), All seismic activity from January 1, 2006, to February 1, 2024. The cyan circles depict 1-month aftershocks, and the red star represents the 2024 M_W 7.5 earthquake epicenter. The black rectangle outlines the region used in Figure S1. (E), Magnitude-time plot of the JMA catalog events from January 1, 2006, to February 1, 2024, with $M_j \geq 1.0$. The red line indicates the cumulative number of events. Events following larger earthquakes during the swarm are color-coded the same as in the maps.

sequence occurring in close space-time proximity to a deeper long-duration swarm, raising questions about the role of fluids and stress changes from the swarm in triggering the damaging shallow earthquake (Normile, 2024; Shelly, 2024; Ishikawa and Bai, 2024). We determine the space-time slip distributions for the largest two events by inverting seismic and geodetic observations and, for the 2024 event, modeling tsunami recordings, and exploring the possible mode of mainshock interaction with the swarm activity, as well as the specificity of the rupture evolution.

2. Datasets and methodology

2.1. Teleseismic data

Based on criteria of high signal-to-noise ratio and evenly distributed azimuthal coverage within teleseismic distances ranging from 30° to 90°, we selected 85 *P*-wave and 45 *SH*-wave teleseismic waveforms for the January 1, 2024 M_W 7.5 Noto earthquake from the Incorporated Research Institutions for Seismology (IRIS) data management center (Fig. 2A). Subsequently, instrument responses were removed to obtain ground displacements within the frequency passband of 0.005 to 0.5 Hz, with a duration of 100 s. Finally, we manually aligned all the *P* and *SH* wave initial motions.

2.2. Geodetic data

For the May 5, 2023 M_W 6.2 Noto event, we estimated the coseismic displacements at three GNSS sites (Fig. S3A) sourced from Japan's GNSS Earth Observation Network System (GEONET), as reported by the Geospatial Information Authority of Japan (GSI). For the January 1, 2024 M_W 7.5 Noto event, we gathered coseismic displacements from 71 GNSS sites (Fig. 2A) within Japan's GEONET, which were processed by both the Nevada Geodetic Laboratory and GSI independently.

We collected available SAR images to derive the coseismic displacements produced by the 2023 M_W 6.2 and 2024 M_W 7.5 Noto events, and more details are shown in Table S1. For the 2023 event, a descending pair of C-band Sentinel-1 SAR images was used in this study. We employed the two-pass differential interference method to derive the coseismic displacements. Due to heavy decoherence effects caused by the steep topography and abundant vegetation coverage in the epicentral region l-band ALOS-2 SAR images were utilized for the 2024 event. These l-band SAR images include two ascending pairs and one descending pair within Stripmap fine mode. Considering the high spatial resolution of these l-band SAR images and the large surface displacement caused by the 2024 event, both the two-pass differential interference and the pixel offset tracking (POT) methods were employed to fully exploit these SAR images for deriving the coseismic deformation (He et al., 2019). All the SAR data for the 2023 and 2024 events were processed based on the Switzerland GAMMA platform (Wegnüller et al., 2016).

We obtained one interferogram for the 2023 event (Fig. S3B), three interferograms, and three range offset images for the 2024 event (Fig. 2B to G), respectively (Table S1). For the 2023 event, the coseismic interferogram exhibits displacements ranging from −0.9 cm to 16 cm in the line of sight (LOS) direction. For the 2024 event, the possible ionospheric disturbance contribution in these l-band interferograms has been corrected following previous studies (Chen and Zebker, 2014). Then, we acquired three interferograms and three range offset images (Fig. 2B to G). Notably, the range offset observations derived from SAR amplitude exhibit consistent deformation trends in the line of sight (LOS) as the interferograms, indicating no systematic errors. It is worth noting that the range offset observations reveal significantly more near-field deformation compared to the interferograms. This enhanced detection is attributed to the ability of range offset observations to overcome incoherence caused by phase unwrapping between adjacent pixels, assuming a 2π phase gradient (He et al., 2019). The interferograms and range offset observations reveal coseismic displacements ranging from −46.6 cm to 423.1 cm in the LOS direction.

We have also estimated the uncertainties associated with these coseismic deformation images by adopting a 1-D covariance function (Parsons et al., 2006), as summarized in Table S1. The Sentinel-1 interferogram for the 2023 event demonstrates a root mean square error (RMSE) of 4.2 cm. As for the 2024 event, ALOS-2 interferograms indicate RMSEs ranging from 8.4 cm to 15 cm. Benefiting from these stripmap SAR images with a high range pixel resolution of ~1.4 m, the range offset observations reveal a commendable quality of the interferograms, with uncertainties measuring <15 cm (Table S1). Finally, these range offset images and interferograms are down-sampled. Specifically, there are 435 points retained for the 2023 event, and a total of 2416 points for the 2024 event.

2.3. Strong-motion data

We selected three-component strong motion waveforms recorded at 28 stations for the 2023 event and 27 stations for the 2024 event, respectively, operated by K-NET, KiK-net, and JMA within epicentral distances of <150 km (Fig. 2A). Near-field strong motion records often suffer from baseline shifts, which can obscure true ground velocities and displacements during integration. In this study, we integrated the accelerations to velocity by removing baseline drifts, following the methodology developed by Wang et al. (2011) and Liu et al. (2023a). Some nearby strong motion data for the 2024 event were excluded due to significant sediment reverberations (ISK002) and uncorrectable baseline drift associated with the 2024 mainshock (ISKH01). Subsequently, the selected data were bandpass filtered between 0.01 Hz and 0.5 Hz for the 2023 event and between 0.01 Hz and 0.3 Hz for the 2024 event, respectively, to eliminate long-period noise and address the limitations of the theoretical model at higher frequencies.

2.4. Finite fault inversion

An integrated analysis of seismic and geodetic data generally proves highly effective in unraveling the rupture process of larger earthquakes. In this study, we employed both data types to investigate the rupture process of the 2023 M_W 6.2 and 2024 M_W 7.5 Noto earthquakes, utilizing a single fault constrained by the distribution of aftershocks and relocations (Yoshida et al., 2023b; Kato, 2024). We used a nonlinear finite fault inversion method (Ji et al., 2002, 2003) to determine the history of kinematic rupture. The model and inversion parameters for these two earthquakes are provided in Table S2. All Green's functions for statics and waveforms were calculated using a regional 1D velocity model (Fig. S2; Nakajima, 2022).

Joint inversions always present challenges in assigning relative weights to different datasets, mainly due to the highly uneven distribution of near-field datasets (Fig. 2 and Fig. S3). In this study, considering the characteristics of the various datasets, we adopted a trial-and-error approach to test various weight assignments for different datasets, guided by independent tsunami simulations (Bai et al., 2022; Liu et al., 2023b). Ultimately, we allocated a weight of 3/4 to the statics relative to the seismic waveforms. Moreover, we assigned three times the weight to the hanging wall recordings for the strong motion data compared to those surrounding the fault.

2.5. Tsunami modeling

NEOWAVE (Nonhydrostatic Evolution of Ocean WAVE) is built upon a depth-integrated non-hydrostatic free-surface flow system with the ability to resolve weakly dispersive waves (Yamazaki et al., 2009, 2011; Bai and Cheung, 2013; Bai et al., 2018). The embedded vertical momentum equation enables the modeling of kinematic tsunami generation from seafloor deformation and tsunami-induced flows over steep continental slopes. These characteristics allow NEOWAVE to compute

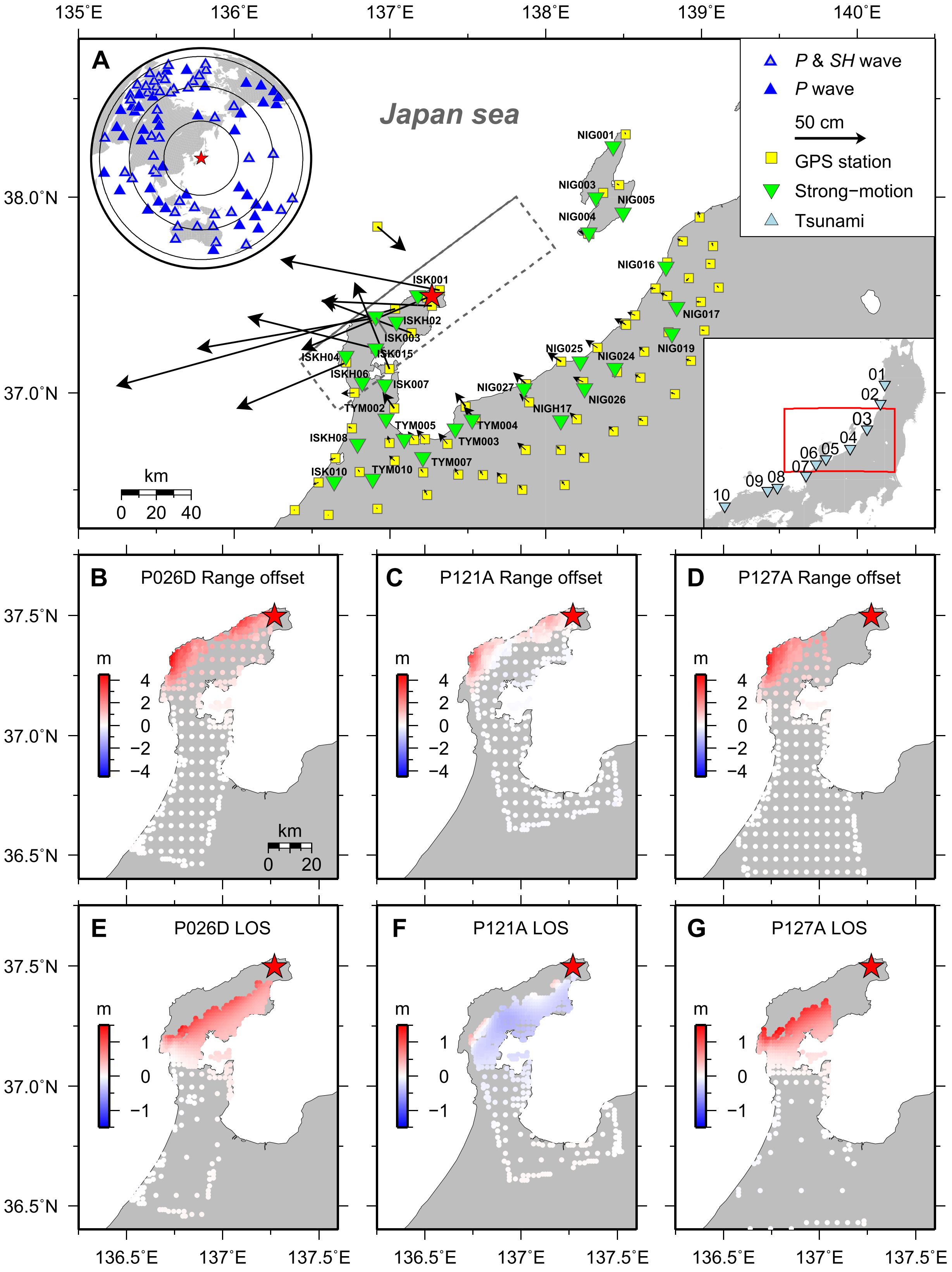

Fig. 2. The distribution of different data sets used in the January 1, 2024 M_W 7.5 mainshock joint inversion. (A), Inverted green triangles indicate strong motion stations, and blue squares indicate GNSS stations used. Black vectors indicate GNSS static horizontal displacements. The inset on the top left shows the distribution of teleseismic body waves, and the lower right shows the locations of the Ultra-sonic seafloor pressure wave gauges. The gray dashed rectangle indicates the assumed fault model used in this study, with a solid line depicting the shallow edge. (B), (C), and (D). depict the InSAR range offset observations obtained from the ascending and descending paths. (E), (F), and (G) indicate the coseismic unwrapped InSAR LOS displacements along the ascending and descending paths.

initial waveforms in the near field (Wei et al., 2024) and accurately reproduce tide gauge or pressure sensor records along coastlines (Bai et al., 2023). The evolution of seafloor deformation at the source is computed from the earthquake finite-fault model through an elastic half-space solution (Okada, 1985) and augmented by the horizontal motion from the seafloor slope (Tanioka and Satake, 1996). The model is discretized on a staggered finite difference grid in spherical coordinates with the implementation of a shock-capturing scheme for bore propagation and two-way nested computational layers for data communications.

A one-level computational domain is set up to model tsunami generation and propagation in the event. The level-1 grid extends across the Sea of Japan at 30-arcsec (~925 m) resolution and adequately describes insular shelves and coastal features along the west coast of Japan. A combined 0.5-*sec* time interval yields optimal dispersion properties for trans-basin tsunami modeling (Li and Cheung, 2019). A Manning coefficient of 0.025 accounts for the sub-grid roughness in the nearshore region. The 1-min water level records are obtained from ten Ultra-sonic wave gauges deployed offshore by the Ministry of Land, Infrastructure, Transport, and Tourism, Japan (Fig. 2A), bandpass filtered to remove wind wave and swell components. Compared to tide gauge measurements, the recorded signals avoid interferences from complex harbors and waterways and become ideal for resolving tsunami waves. The digital elevation data GEBCO is utilized to construct the topography and bathymetry.

3. Results

3.1. Rupture initiation behavior of large shallow earthquakes along the Noto peninsula

The occurrence of large shallow crustal faulting above a deeper long-duration patchy seismic swarm is very unusual and prompts inquiry into the causal interactions between the processes. We first consider the very early stage of rupture of the shallow crustal events, including the 2007 M_W 6.7 rupture at the western end of the peninsula and four large events from 2021 to 2024 located directly above the swarm (Fig. 3A). The initial seismic radiation for each event is well-recorded by local strong-motion stations along the peninsula (Fig. 3A to F). The seismic ground accelerations have been shifted for travel time move-out to align the first arrivals on 10 s in each profile.

The 50 s long profiles clearly show substantial, 15 to 20 s delays of large arrivals for the January 1, 2024 event (Fig. 3F), for which the US Geological Survey origin time is 07:10:09.48 UTC. The zoomed-in profiles spanning 2.5 s indicate that the 2007 event has weak first arrivals in the first 0.4 to 0.6 s at all distances (Fig. 3B), so a sluggish growth of rupture may be associated with the ascent of fluids (not directly associated with swarm activity) noted in the introduction. The September 16, 2021 event has relatively typical early *P* wave energy (Fig. 3C) for a crustal event, whereas the June 19, 2022 rupture has unusually large low-frequency energy in the first 0.6 s of rupture (Fig. 3D). The May 5, 2023 event has weak arrivals in the first 0.6 s (Fig. 3E) similar to those of the 2007 event. The January 1, 2024 major event has very weak initial energy in the first 1 s of rupture (Fig. 3F), suggesting either a gradual nucleation process or occurrence of one or more immediate small foreshocks (the Japan Meteorological Agency catalog lists two small events about 14 s ahead of a 7.5 event at 07:10:22.57 UTC). For the four events above the swarm, the temporal evolution of early rupture characteristics may reflect the accumulation of fluids rising from the source region into the shallow crustal fault system, with progressive impact on the larger event nucleation from 2021 to 2024. High-resolution earthquake locations indicate that the 2022 and 2023 events likely ruptured the same fault from deeper to shallower (Kato, 2024) (Fig. S1), so the unusual long-period energy for the 2022 event originated within the swarm region, and fluid weakening may have affected its nucleation. We proceed to analyze seismic, geodetic, and tsunami data to determine the complete rupture process for the large 2023 and 2024 events.

3.2. Rupture kinematics of the May 5, 2023, M_w 6.2 earthquake

The magnitude 6.2 earthquake on May 5, 2023, initiated up-dip of the Noto seismic swarm, and was accompanied by numerous shallow aftershocks (Kato, 2024). The event was well recorded by regional strong-motion stations, Interferometric Synthetic Aperture Radar (InSAR), and Global Navigation Satellite System (GNSS) stations (Fig. S3), providing data to determine the space-time slip distribution. We constructed a single rectangular fault model with 2 km by 2 km subfaults, with a strike of 53° and southeastward dip of 42°, as constrained by relocated aftershocks (Yoshida et al., 2023b; Kato, 2024) (Fig. S1E), and set the hypocenter beneath the relocated epicenter (37.534°N, 137.306°E) at a depth of 12.5 km (Yoshida et al., 2023b). Employing a simulated annealing-based nonlinear finite fault inversion method, we jointly inverted geodetic and strong-motion observations, using the inversion parameters listed in Table S2.

The preferred coseismic slip distribution of the 2023 M_W 6.2 event is displayed in Fig. 4, and the corresponding fits to geodetic displacements and strong motion waveforms are provided in Fig. 4 and Figures S4 and S5. The model features a dominant deeper large-slip patch and a weaker shallow one, distributed up-dip of the hypocenter, contributing to a total seismic moment of $M_0 = 3.6 \times 10^{18}$ Nm. The main slip zone is confined within the depth range of 5–14 km, with a peak slip of ~2.8 m, and the total rupture duration is ~10 s (Fig. 4). While most aftershocks fringe the large-slip regions, there is moderate overlap with the deeper large-slip patch (Fig. 4), indicating that the mainshock did not fully release all the built-up stress in the fault zone. This highlights likely non-uniformity in fault properties, such as frictional resistance or mechanical strength along the fault plane, which can cause irregular rupture during the coseismic slip. Alternatively, continuous fluid migrations along the fault can exacerbate the weakening of the fault zone.

The preferred model produces acceptable fits to both coseismic GNSS statics and InSAR data (Fig. 4 and Fig. S4), although some detailed features in the InSAR data do not fit precisely, potentially due to the presence of noise and artifacts in the measurements. The model accounts for the dominant portions of the strong motion ground velocity records well (Fig. S5); however, some high-frequency waveform misfits are present, reasonably attributable to local 3D site effects that are not included in our modeling.

3.3. Rupture kinematics of the January 1, 2024, M_w 7.5 earthquake

The M_W 7.5 earthquake on January 1, 2024, is the largest event recorded along the Noto Peninsula, comparable in size to major events along the eastern edge of the Sea of Japan offshore of Honshu and Hokkaido to the north with complex rupture (Ishikawa and Bai, 2024; Fujii and Satake, 2024; Okuwaki et al., 2024; Masuda et al., 2024; Yang et al., 2024; Ma et al., 2024; Xu et al., 2024). Although it nucleated near the ongoing Noto swarm, this mainshock rupture is shallower and extends well beyond the extent of the swarm (Fig. 1D). Ground motion recordings acquired directly above the rupture zone present a valuable opportunity to determine the precise slip distribution of the onshore portion of the event, and many seismic stations, geodetic sensors, and seafloor pressure sensors along the coast allow the offshore rupture to be well resolved. Employing a similar approach to that for the M_W 6.2 earthquake, and guided by the distribution of aftershocks and a well-determined fault plane (Kato, 2024) (Fig. S1), we construct a single rectangular fault model with 5 km by 5 km subfaults, with strike of 53°, southeastward dip of 42°, and hypocenter at a depth of 15.23 km with the JMA 7.5 mainshock epicentral coordinates of 37.496°N, 137.270°E, and an origin time 07:10:09 UTC (consistent with teleseismic *P* arrival times and the USGS-NEIC origin time, and within ±1 s of the JMA 'nucleation phase' at 07:10:08.3 and a 5.9 'foreshock' at 07:10:09.54 at depths of 10.1 km). While some studies have introduced various fault

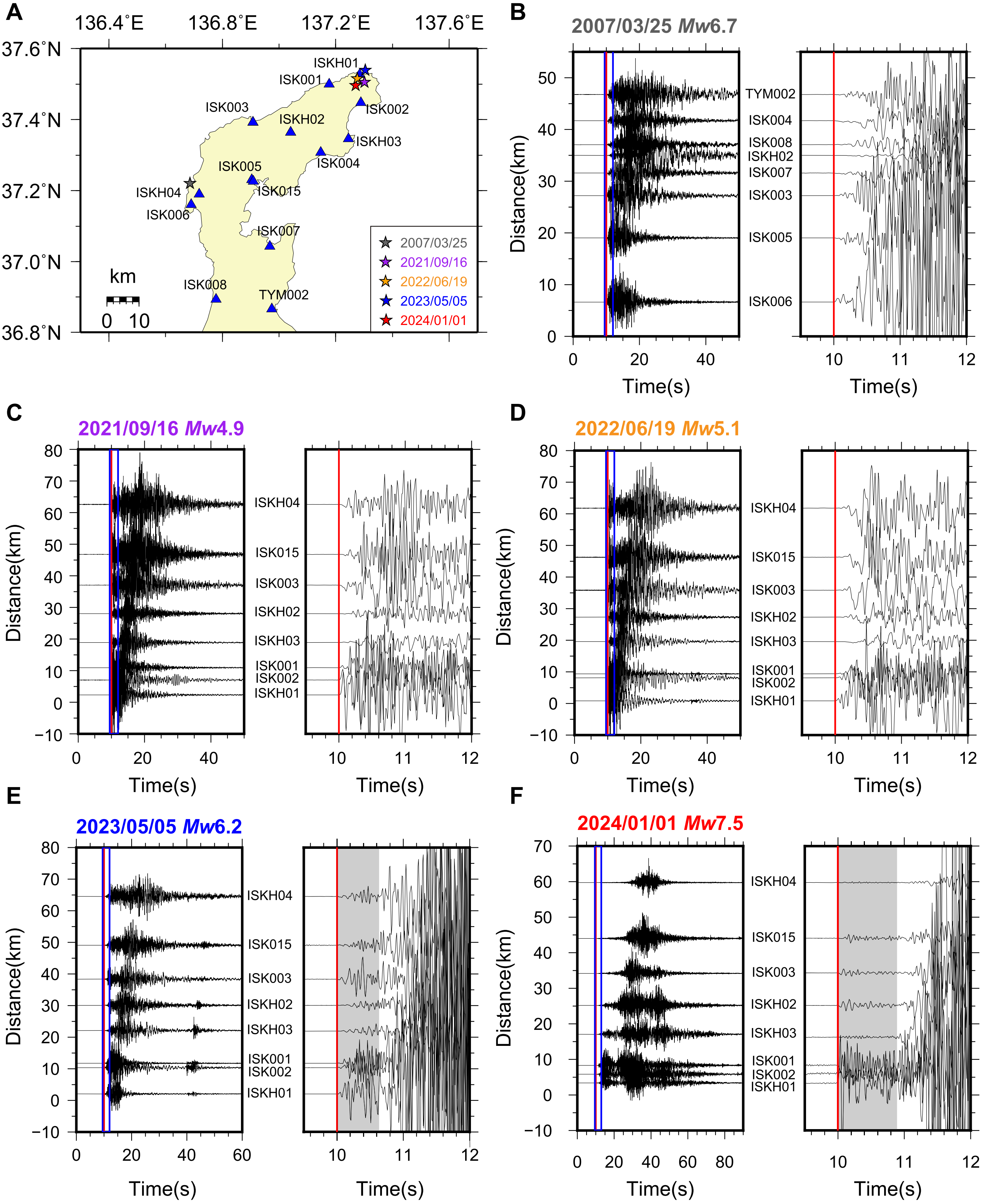

Fig. 3. Nearby seismic radiation for larger shallow crustal events beneath the Noto Peninsula. (A), Triangles indicate the locations of strong-motion stations used to analyze the very early rupture stage. Stars indicate the earthquake epicenters. (B)-(F), Profiles of seismic ground acceleration, shifted for travel time move-out to align the first *P* arrivals on the red lines at 10 s. The left panels show 50–80 s time windows, and the right panels show zoomed-in profiles spanning 2.5 s, highlighted with two vertical blue lines in the left panels.

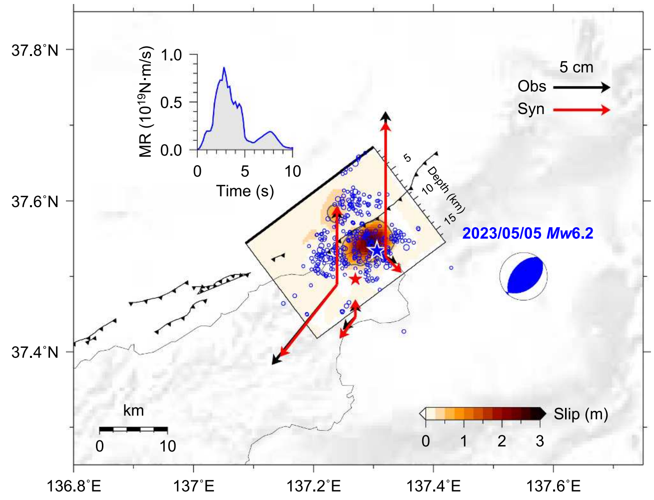

Fig. 4. Joint inversion finite-fault model for the May 5, 2023 M_W 6.2 earthquake. The red and blue stars represent the epicenters of the January 1, 2024 M_W 7.5 and May 5, 2023 M_W 6.2 earthquakes, respectively. The gray line indicates the 0.5 m slip contour, and the blue circles mark relocated aftershocks with a magnitude of $M_j \geq 2.5$ (Kato, 2024). The blue focal mechanism represents the moment tensor derived from this study. Active faults are depicted with black barbed lines, and the inset shows the moment-rate function (MRF) of the joint slip model. Black and red vectors indicate observed and synthetic coseismic geodetic displacements, respectively. Fits to InSAR and strong-motion data are shown in Figures. S4 and S5.

segments with changes in strike and/or dip, the offshore geometry is not tightly constrained by aftershock locations, and complexity of the fault system is not resolved. Our model fits the aftershocks quite well (Fig. S1) and is sufficient to fit teleseismic and regional observations very well, so we prefer the single plane representation. We believe the rupture process commenced significant moment release at about 07:10:09 UTC and grew rapidly around 07:10:23. Fitting to our model grid adjusts the depth slightly, but ensures that the mainshock energy originates in the hypocentral grid. We determine coseismic slip models by separately or jointly inverting teleseismic waveforms, strong-motion waveforms, GNSS statics, and InSAR data. Key inversion parameters are listed in Table S2. The resulting slip models are evaluated through tsunami modeling, iteratively adjusting data weighting to develop a preferred joint model. Inversions performed using hypocentral parameters based on the JMA nucleation phase or the JMA 5.9 foreshock give nearly identical results. Small variations in precise origin time of 1 s and precise onset depth of a few kilometers are simply not resolved in the discretized finite-fault models when the onset of slip is emergent and weak as in this case. Our slip inversions are robust relative to the chosen parameters.

We initially perform finite-fault inversions separately using teleseismic body wave ground displacements or regional strong-motion ground velocity seismograms (Figs. S6 to S8). These two slip models indicate bilateral shallow ruptures, with large-slip regions fringed by the deeper distribution of aftershocks (Fig. S6). The teleseismic model has a more uniform slip pattern than the strong-motion model, with a peak slip of approximately 5.5 m (Fig. S6A). The slip distribution of the strong motion model has higher spatial resolution and indicates notable non-uniformity, with a peak slip of ~8.5 m, located up-dip of the hypocenter (Fig. S6B). It is important that our inversions for both data sets allow a wide range of rupture velocities and rise time for each position on the fault (Table S2) as slow initial rupture expansion (< 1 km s^{-1}) places large slip near the hypocenter. Kinematic models for each data set with imposed higher rupture velocities tend to have little slip near the hypocenter (Ishikawa and Bai, 2024). The total seismic moment estimated from these slip models is consistently ~2.5 × 10^{20} Nm, which is about 10 % larger than the USGS *W*-phase moment tensor solution (2.268 × 10^{20} Nm) but comparable to the GCMT solution (2.47 × 10^{20} Nm). The estimated rupture duration is about 80 s for both inversions. Both models effectively capture the primary characteristics of teleseismic and strong motion waveforms, with the exception of some misfits of high-frequency signals (Figs. S7 and S8), again likely due to overly simplified structural models. Next, we combine the data sets in joint seismic and seismic-geodetic models.

The 2024 Noto earthquake has superb geodetic data sets from GNSS and InSAR observations (Fig. 2A to G), that provide excellent constraints on the coseismic slip beneath the peninsula. For ruptures that extend from below land to offshore, as in this case, unevenly distributed InSAR and GNSS measurements can potentially introduce bias in slip model inversions (Liu et al., 2015). To explore this issue, we perform separate inversions of the combined teleseismic and strong-motion data set or the combined GNSS and InSAR geodetic data set. The validity of the separate slip distributions is then evaluated using modeling of the regional tsunami recordings at seafloor pressure sensors along the coast (Fig. 2A). The separately inverted seismic and geodetic slip models are shown in Fig. 5, and both models can explain the separate sets of observations well (Figs. S9 and S11). The joint seismic kinematic model exhibits similar features to the separate teleseismic and strong-motion models (Fig. S6),

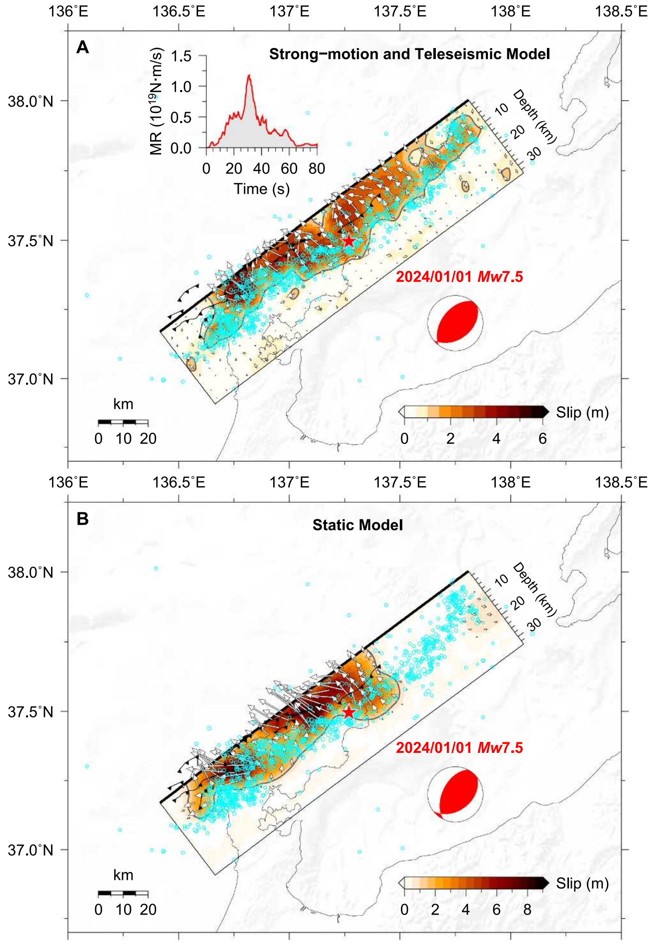

Fig. 5. Finite-fault models from seismic or geodetic data sets for the 2024 M_W 7.5 earthquake. (A), Seismic slip model determined by inversion of the joint strong-motion and teleseismic data. The inset shows the moment-rate function (MRF) of the seismic model. (B), The slip model was inverted using the geodetic static displacements. The gray contours in each model highlight the 1 m slip, and white arrows indicate the direction of the slip. The cyan circles mark 1-month aftershocks with a magnitude of $M \geq 3.0$, from the JMA catalog. The red focal mechanisms represent the moment tensor for the corresponding finite-fault models. Black barbed lines represent active faults. All seismic waveform fits are shown in Figures S9 and S10, and geodetic fits are shown in Figure S11.

with a slightly asymmetric bilateral slip distribution. The geodetic static slip model has a predominantly unilateral southwestward rupture, with little slip detected to the northeast, which is a predictable bias from the data distribution. To provide an assessment of the offshore slip, Figures S12 and S13 illustrate comparisons between the observed tsunami waves at the seafloor sensors in Fig. 2A and the predictions of the two models in Fig. 5, assuming seafloor motions from kinematic generation for the seismic model and static generation for the geodetic model. Both models reasonably predict the tsunami signals recorded at stations 06–10, located southwest of the epicenter (Fig. 2A), but fail to accurately simulate the onset phase of tsunami waveforms at stations 01–04, positioned northeast of the epicenter (Fig. 2A). This discrepancy is attributed to insufficient seafloor uplift on the northeast side of the fault for both models.

The difference between seismic and geodetic models in Fig. 5 highlights the formidable challenge of accurately constraining the slip model by simultaneously inverting both types of data. The relative weighting of the different observations always poses a significant challenge for joint inversions, and this is exacerbated by the strong bias in the spatial coverage of the geodetic data. We conduct tests for various weighting scenarios to determine the optimal choice for each dataset in the joint inversion, with the prediction of tsunami observations guiding our final choice. Because tsunami excitation is sensitive to the spatial distribution of seafloor uplift, it balances the dense on-land sampling of ground displacement from the geodetic observations, so the full model can be well resolved. The ultimate slip model is shown in Fig. 6, with details in Figure S14A. The rupture has asymmetric bilateral propagation dominated by a significant shallow slip concentration of up to ~8 m under the Noto Peninsula, with large slip in the depth range of 0 to 16 km, and a total rupture length of ~150 km. The slip distribution exhibits significant patchiness, featuring two distinct large-slip asperities located below the peninsula and smaller patches of up to 3 m slip offshore to the northeast (Fig. 6). Rake on the fault varies modestly, with the patchiness and obliquity allowing the solution to account for the strong strike-parallel component of geodetic surface displacements (Fig. 7). The cumulative seismic moment is 2.5 × 10^{20} Nm, consistent with the long-period GCMT point-source solution (2.47 × 10^{20} Nm), and the average focal mechanism depicted in Fig. 6 closely resembles the best double-couple solution (with a strike 49°, dip 41°, and rake 102°) derived from the long-period moment tensor inversion by the USGS-NEIC.

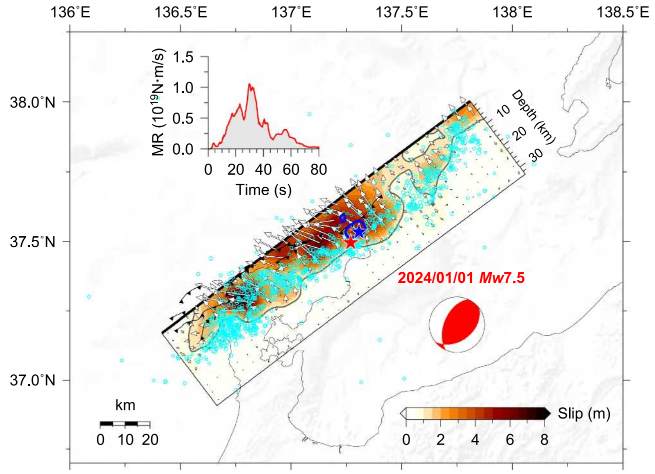

Fig. 6. The final slip model from joint inversion of all data sets for the 2024 M_W 7.5 earthquake. The red and blue stars represent the epicenters of the 2024 M_W 7.5 earthquake and 2023 M_W 6.2 earthquake, respectively. The gray contour highlights the 1 m slip, while the blue contours delineate the ≥ 0.5 m slip zone of the 2023 M_W 6.2 event. White arrows indicate the direction of the slip, and cyan circles show 1-month aftershocks with a magnitude of $M \geq 3.0$ from the JMA catalog. The inset shows the moment-rate function (MRF) of the final slip model. The red focal mechanism represents the moment tensor derived from this fault model. Black barbed lines represent active.

Snapshots of the space-time slip evolution indicate two-stage rupture that slip spread slowly at from 0.5 to 1.0 km s^{-1} up-dip of the hypocenter during the first 20 s (Fig. S15), then the rupture expanded asymmetrically to the southwest at about 1.3 km s^{-1}, with a general decrease in rise time (Fig. S14B). The very low initial rupture velocity is strongly influenced by the choice of hypocentral time, and could be misleading if the initial radiation is from discrete foreshocks some 13 s ahead of the mainshock, but we infer a gradual rupture growth based on the character of both the nearby strong-motions (Fig. 3) and the slow growth of long-period energy in the teleseismic P waves (Fig. 8). After 30 s, the rupture expanded to the northeast, with a somewhat lower rupture velocity of <1.2 km s^{-1}, corresponding to a larger slip rate (shorter rise time) (Fig. S14C). Most of the seismic moment was released within 80 s (Fig. 6), and the overall average rupture velocity is ~1.2 km s^{-1}. The broadband radiated energy estimated for the event is 2.3 × 10^{15} J (IRIS radiated energy). Utilizing the seismic moment from the preferred slip model, we calculated a moment-scaled radiated energy (E_R/M_0) of 1.08 × 10^{-5}, comparable to the average value of 1.06 × 10^{-5} for interplate thrust events (Ye et al., 2016), and lower than the value of about 3 × 10^{-5} found for Japanese inland earthquakes in the magnitude range 5.6 to 7.0 found by Kanamori et al. (2020). We also calculated the radiation efficiency (η) of the 2024 Noto earthquake using the expression $\eta = 2(E_R/M_0)\mu/\Delta\sigma$ (Ye et al., 2016), obtaining a value of ~0.26. Here, E_R/M_0 is the moment-scaled radiated energy as calculated above; μ is the shear modulus (~2.83 × 10^4 MPa), estimated from the velocity model we used (Fig. S2; Nakajima, 2022); and $\Delta\sigma$ is the average static stress drop (~2.36 MPa), computed from our preferred slip model following using the relation proposed by Kanamori and Anderson (1975).

The model fits for subsets of the geodetic and seismic data are shown in Figs. 7 and 8 (all additional data comparisons are shown in Fig. S16). The preferred slip model satisfactorily matches all observations, including the tsunami signals in both directions along the coast (Fig. 9). Comparing Figs. 5 and 6, this is the result of larger shallow slip along the northeastern portion of the model. The overall fitting to InSAR and GNSS statics is satisfactory, with the exception of several GNSS stations southwest of the epicenter, which have large misfits for all models. These may be attributed to the local influence of early aftershocks, such as an M_j 6.2 event that occurred nearby just 8 min after the mainshock or possibly site slumping during the mainshock. The strong ground motion data generally align well in the main phases; however, the high-frequency signals at several stations remain underestimated, presumably due to local 3D site effects. Overall, the good fits between the extensive observations and synthetics indicate the reliability of our coseismic slip model for the 2024 Noto earthquake.

Additionally, to assess the uncertainty in the slip model for the 2024 Noto earthquake, we also performed ten inversions, each using a different random seed. The results indicate that the large-slip distributions across the ten models exhibit relatively stable behavior, showing strong consistency (Fig. S17A). Overall, the standard deviation (STD) for most fault segments is small, generally <10 % (Fig. S17B). The higher STD observed in certain parts of the fault model is likely due to the lack of very near-fault observations in those areas.

Direct inversion of the tsunami signal at Naoetsu indicates large sea surface displacement of up to 3 m near (just to the southwest) the fault slip patch in our preferred model (Yamanaka et al., 2024), so slip in the northeast may be underestimated by our model. Given the uncertainty in precise fault geometry and velocity models there is ~5–10 km uncertainty in absolute location of the northeastern slip patch.

4. Discussion and conclusions

Many researchers have proposed slip models for the 2024 M_W 7.5 Noto earthquake based on seismic data (Okuwaki et al., 2024), geodetic observations (Yang et al., 2024), tsunami waveforms (Masuda et al., 2024; Yamanaka et al., 2024), and joint inversion of multiple datasets

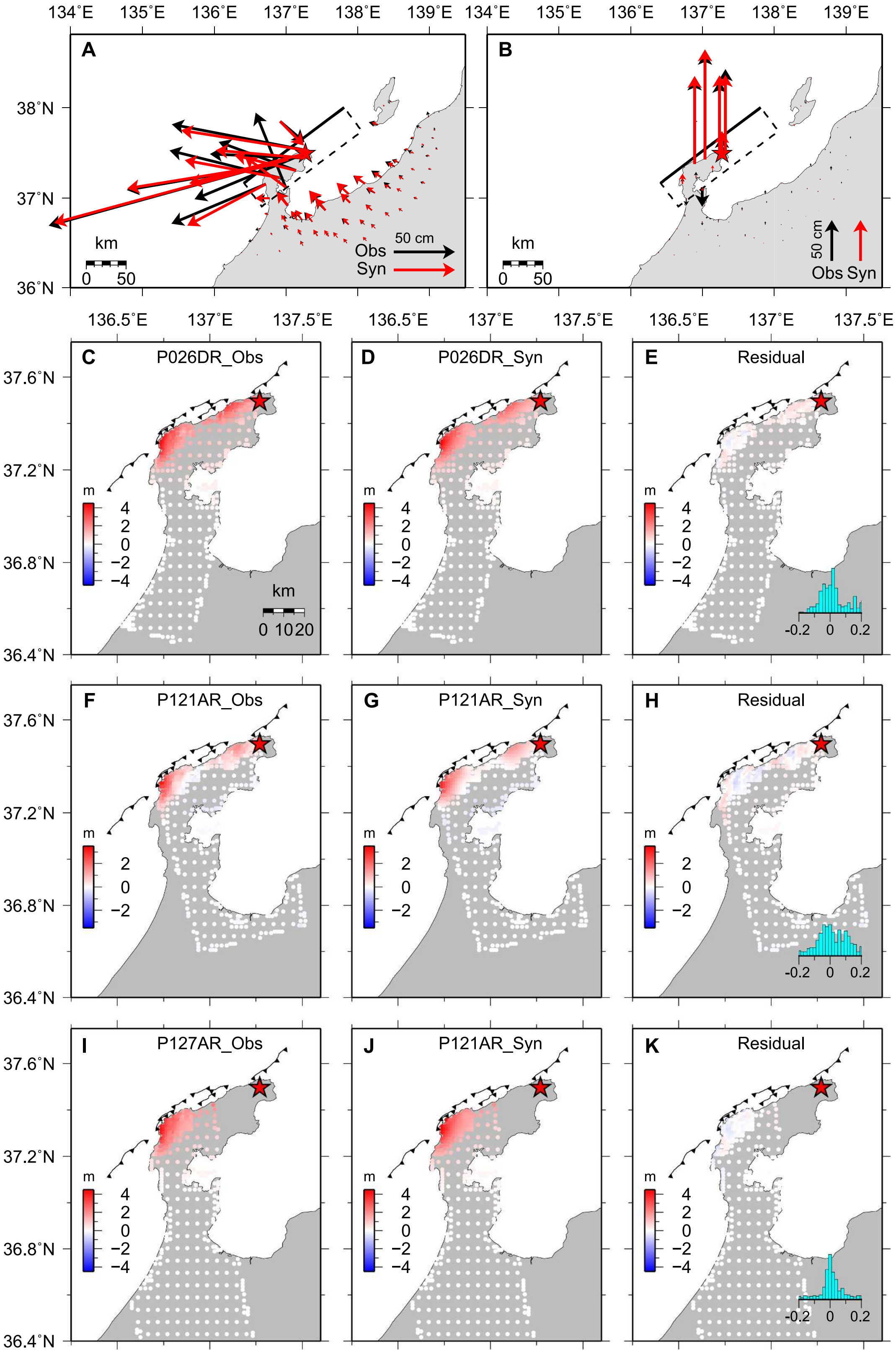

Fig. 7. Comparison of subsets of the observed geodetic data and predictions for the preferred slip model in Fig. 6. (A) and (B). depict the horizontal and vertical GNSS displacements, respectively, with observed data in black and predictions in red for the preferred slip model shown in Fig. 6. The gray dashed rectangle indicates the assumed fault model used in this study, with the shallow edge depicted by a solid line. (C), (F), and (I) show the range offset of the descending track P026 and ascending tracks P121 and P127, respectively. (D), (G), and (J) indicate the corresponding predictions of range offsets derived from the preferred joint slip model. (E), (H), and (K) show residuals of range offsets along the ascending and descending paths, respectively. The active faults are denoted by black barbed lines, with the 2024 M_W 7.5 earthquake epicenter marked by a red star. InSAR LOS data fits are shown in Figure S16A.

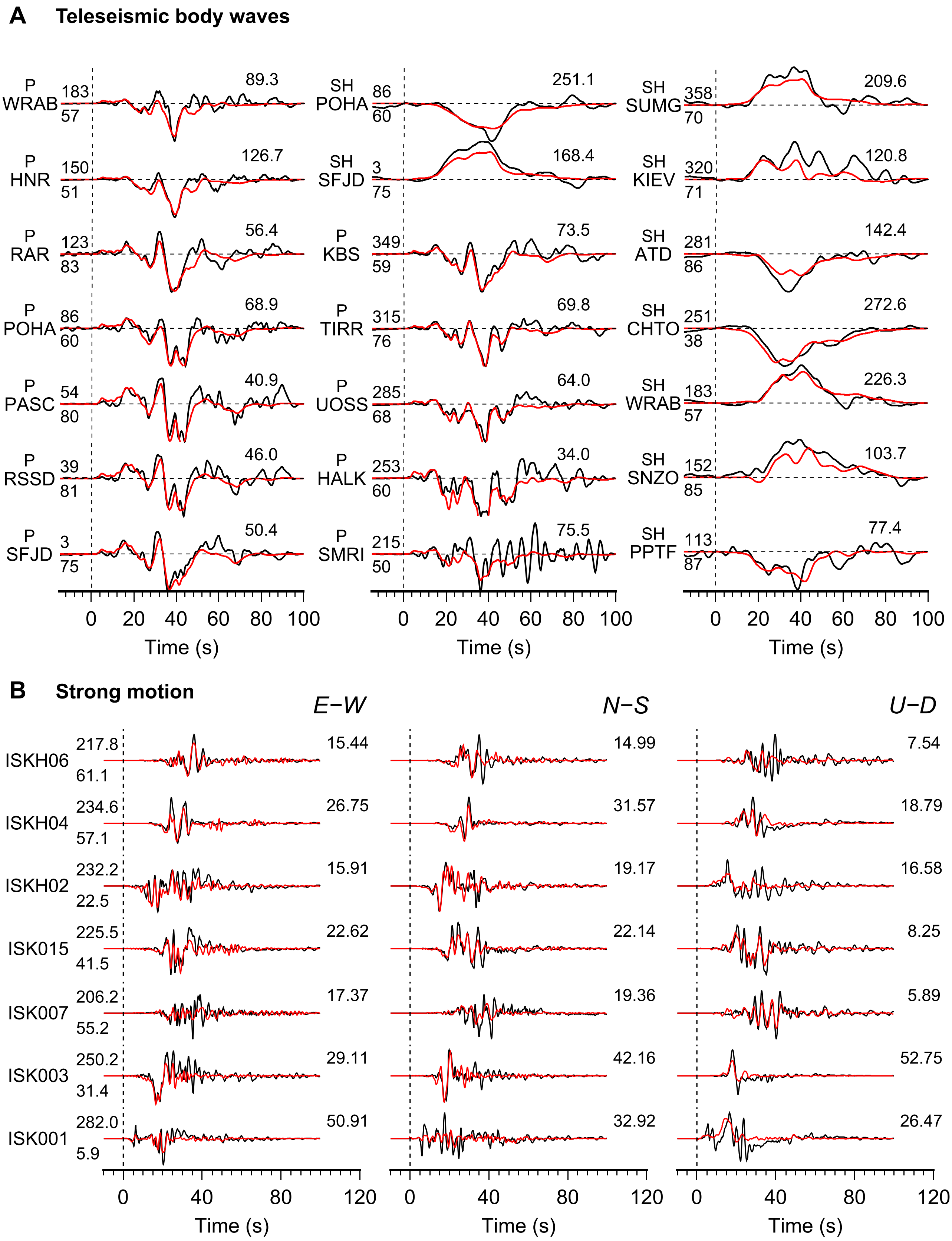

Fig. 8. Comparison of subsets of the observed seismic data and synthetics for the preferred slip model in Fig. 6. (A) and (B), Example comparisons of teleseismic ground displacement and strong-motion ground velocity signals, respectively. The azimuth and epicentral distance for each station are denoted above and below the onset of the waveform, respectively. The number at the end of each record represents the peak value in μm for teleseismic data and in cm/s for strong-motion data. All additional data fits are shown in Fig. 15, B to D.

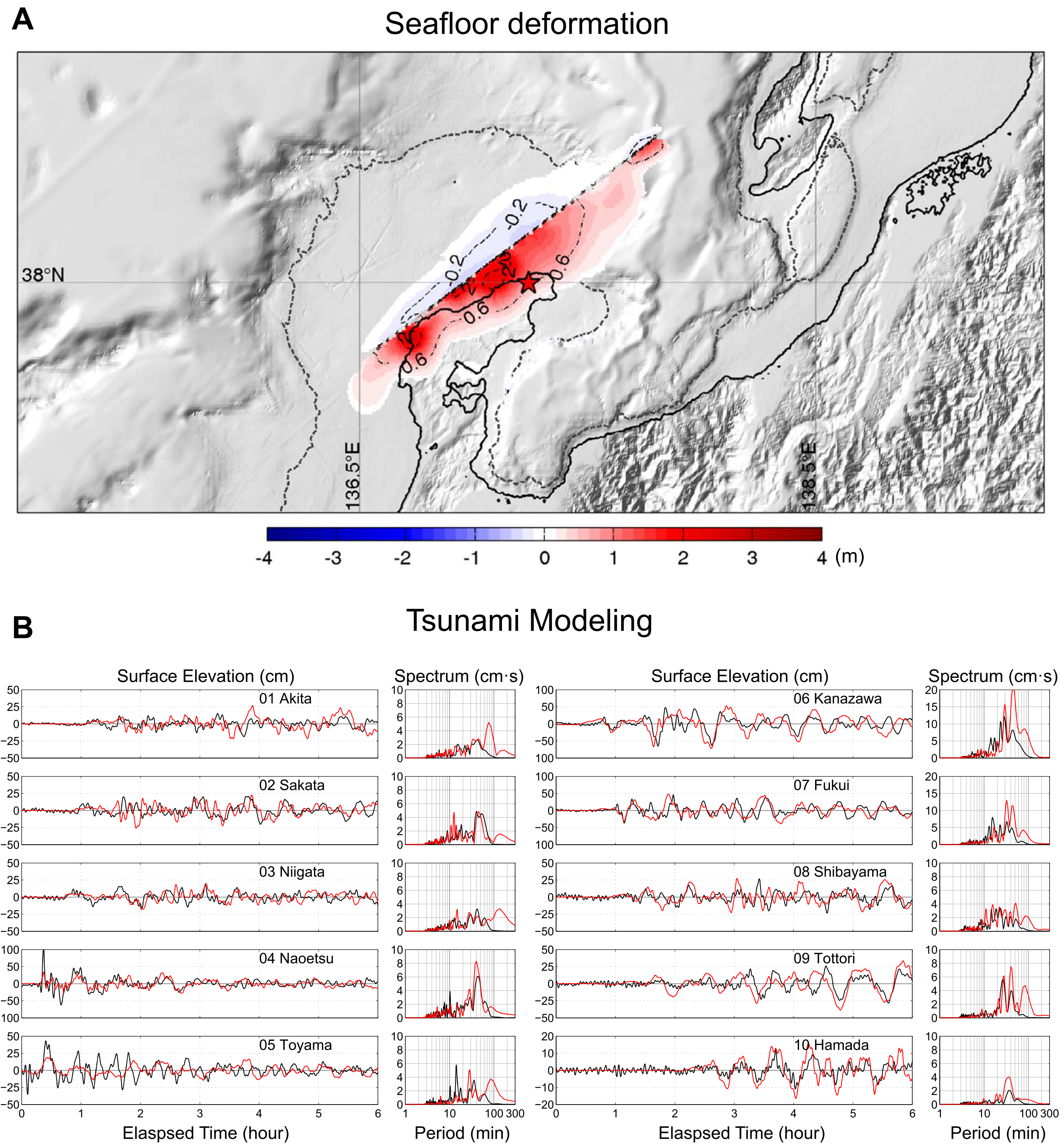

Fig. 9. Tsunami predictions for the preferred slip model in Fig. 6. (A), Vertical seafloor and land surface deformation computed for the final model. (B), Comparison of tsunami waveforms and predictions at the seafloor pressure stations shown in Fig. 2A. Black lines represent observed time series (left) and amplitude spectra (right), while the predictions are indicated by red lines.

(Fujii and Satake, 2024; Ma et al., 2024; Xu et al., 2024). These models have used a variety of different fault system geometries, which are at best weakly suggested by the locations of offshore aftershocks and are not clearly justified, as we are able to reconcile all data with a uniform single fault geometry. Okuwaki et al. (2024) analyzed teleseismic waveforms and identified four distinct rupture episodes on differently oriented fault segments. Yang et al. (2024) performed a geodetic inversion and found two slip patches, with a maximum slip of ~4 m extending to the trench. Fujii & Satake (2024) inverted tsunami waveforms and GNSS data using a coarse fault-segment model, identifying a peak slip of ~3.5 m located along the northern coast of the Noto Peninsula. Ma et al. (2024) and Xu et al. (2024) conducted a joint inversion of seismic and geodetic datasets using three fault segments and incorporated teleseismic back-projection analysis to investigate rupture velocity.

The first rupture phase in our model, characterized by a slow rupture velocity, is consistent with the findings of Ma et al. (2024) and Xu et al. (2024). The slip model proposed by Ma et al. (2024) shows a peak uplift of 5 m on the west coast and shallow slip exceeding 10 m on an offshore fault. The slip model of Xu et al. (2024), on the other hand, reveals significant complexity in the early stages of rupture, including a double-pincer rupture front and an extreme non-uniform slip distribution. However, neither of these models adequately resolves the slip in the northeastern part of the fault. Our preferred slip model integrates all datasets and reveals a heterogeneous slip distribution, with a peak slip of ~8 m and significant slip extending into the northeastern segment of the fault. To verify the presence of slip in this region, we modeled the tsunami waves generated by the slip models of Ma et al. (2024) and Xu et al. (2024). A key difference is that, despite incorporating complex fault representations, their models fail to accurately reproduce the observed tsunami waveforms, particularly at the Naoetsu station (Fig. S18). By resolving slip in regions previously undetermined, particularly in the northeast, our study provides a more comprehensive understanding of the rupture process and its impact on tsunami generation, emphasizing the importance of capturing subtle but critical variations in slip distribution for realistic tsunami simulations.

The most distinctive features of the January 1, 2024 M_W 7.5 Noto earthquake are the slow nucleation within the depth range of the ongoing Noto swarm, the very low initial rupture expansion at < 1 km s^{-1} during the first 20 s of weak seismic radiation, and the low average rupture velocity of $\sim$1.2 km s^{-1} for the overall bilateral rupture. The May 5, 2023 M_W 6.2 event ruptured in the region of the larger event nucleation on either the same fault or on a slightly offset parallel plane (Fig. 10). Future precise relocation of aftershocks may resolve this question. That event also had a gradual nucleation process, as was the case for the 2007 M_W 6.7 event southwest of the swarm region. The initiation of the 2024 mainshock occurred at the boundary of the slip area of the 2023 M_W 6.2 Noto earthquake (Fig. 4), suggesting that stress transfer from the 2023 event may have contributed to triggering the 2024 mainshock. Previous studies (Kato et al., 2011; Amezawa et al., 2023; Yoshida et al., 2023a, 2023b) have proposed that the long-term Noto Peninsula seismic swarms and the 2023 earthquake were influenced by fluid pressure migrating upward along a pre-existing fault, based on detailed spatio-temporal patterns of seismicity. It is plausible that much of the shallow thrust fault activated in 2024 has been permeated by fluids from below, both along the swarm region, as suggested in Fig. 10, and along the peninsula. Thus, the 2024 mainshock likely resulted from a combination of long-term seismic swarms, stress activation from the 2023 Noto event, and fluid intrusion, highlighting the complex interaction between tectonic and fluid processes in this region.

The role of fluids in weakening fault zones by increased pore pressure reducing effective normal stress is well-established (Cebry and McLaskey, 2021), but it is less clear to what degree the presence of fluids control rupture velocity, which is primarily controlled by available fracture energy, related to the ratio of shear stress to normal stress and shear stress drop (Dong et al., 2023). Rupture velocity has been experimentally found to increase as the ratio of fluid pressure to normal stress acting on the fault at the onset of rupture decreases (Passelégue et al., 2020). Rupture velocities tend to be lower in regions of low effective normal stress with near-lithostatic fluid pressure (Rice, 1992; Kato et al., 2010; Marguin and Simpson, 2023), and this can contribute to the slow rupture nucleation for the larger events originating close to the swarm, where low stresses are likely. Slip velocity was also found (Passelégue et al., 2020) to increase with rupture velocity, which can produce complex patterns during rupture of heterogeneous fault systems, as appears to be the case for the 2024 event (Fig. S14). Fluid injection has been shown to reactive faulting (Passelégue et al., 2018; Maurer et al., 2020; Cebry and McLaskey, 2021; Gori et al., 2021), with the rate of injection and the permeability and roughness of the fault influencing the development of locally undrained conditions where fluid pressure variations can trigger faulting. While up-dip fluid penetration into the shallow fault system may be widespread along the peninsula, the swarm activity may have increased fluid injection rates, contributing to the large events near the swarm and triggering the 2024 event. Weakening of the shallow fault system overall may account for the relatively low rupture velocity and low radiation efficiency during the 2024 mainshock.

The extensive damage caused by the January 1, 2024 Noto earthquake is directly a result of the large shallow crustal displacements, of up to 8 m, below the densely populated peninsula, but the rupture itself appears to have been influenced by fluids rising from the lower crust, especially in the region of the prolonged swarm near the hypocenter. A low-velocity anomaly is observed beneath the swarm region (Nakajima, 2022), but the origins of the fluids are not clear; they may source from ancient volcanic magma chambers from the former rifting environment, or possibly source from the underlying mantle, which is penetrated by the subducting Philippine and Pacific plates located 200 to 300 km below the Noto Peninsula (Miyazaki et al., 2023). This is a very rare situation in which a compelling case can be made for a crustal swarm producing favorable conditions (up-dip fluid intrusion) to trigger a nearby large destructive mainshock rupture. The occurrence of the 2024 M_W 7.5 Noto earthquake highlights the importance of monitoring the evolution of other earthquake swarms involving fluid intrusion, especially if the crust is under a critical stress state.

Data Availability

All teleseismic body wave records can be obtained from the Federation of Digital Seismic Networks (FDSN: https://doi.org/10.7914/SN/CI, https://doi.org/10.18715/GEOSCOPE.G, https://doi:10.14470/TR560404, https://doi.org/10.7914/SN/IU, https://doi.org/10.7914/SN/II, https://doi.org/10.7914/SN/IC), and accessed through the IRIS data management center (http://ds.iris.edu/wilber3/find_stations/11786236). The estimated far-field broadband radiated elastic energy was reported at IRIS: The estimated far-field

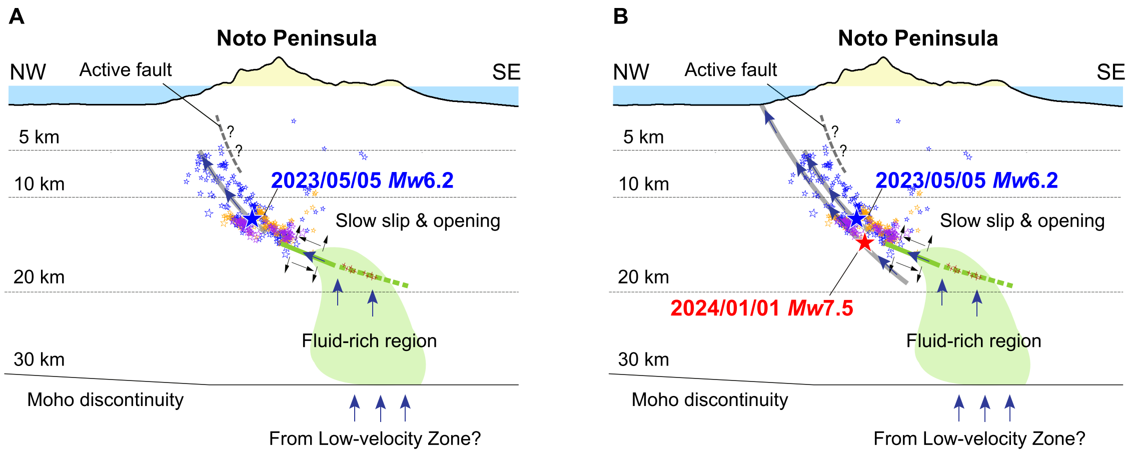

Fig. 10. Schematic diagrams of the earthquake swarm evolution beneath the Noto Peninsula. (A) and (B), illustrate the swarm evolution before and after the 2024 M_W 7.5 earthquake. Magenta, orange, and blue-colored stars indicate the aftershock sequences of the 2021, 2022, and 2023 swarm activities, respectively. Blue- and red-filled stars represent the locations of the 2023 M_W 6.2 earthquake and the 2024 M_W 7.5 earthquake, respectively. Blue arrows denote possible fluid migration pathways, while the potential fluid-recharge regions are indicated by light green shading. These diagrams are based on the work of Kato (Horton, 2012).

broadband radiated elastic energy was reported at IRIS: http://ds.iris.edu/spud/eqenergy/18152286; The strong-motion data can be obtained from K-net, Kik-net and JMA (https://www.data.jma.go.jp/eqev/data/kyoshin/jishin/index.html; https://www.kyoshin.bosai.go.jp/kyoshin/docs/overview_kyoshin_en.shtml); The coseismic GNSS displacements for the 2023 and 2024 earthquakes are available from Nevada Geodetic Laboratory (http://geodesy.unr.edu/index.php) and GSI (https://www.gsi.go.jp/syoukai.html); The JAM catalog are available from https://hinetwww11.bosai.go.jp/auth/JMA/jmalist.php?LANG=en; The 1-min water level records are obtained from the Ministry of Land, Infrastructure, Transport, and Tourism, Japan (MLIT, https://www.mlit.go.jp/en/).

CRediT authorship contribution statement

Chengli Liu: Writing – original draft, Software, Methodology, Investigation, Funding acquisition, Formal analysis, Data curation, Conceptualization. **Yefei Bai:** Writing – original draft, Software, Methodology, Investigation, Formal analysis, Data curation, Conceptualization. **Thorne Lay:** Writing – original draft, Visualization, Validation, Investigation, Funding acquisition, Formal analysis, Conceptualization. **Ping He:** Writing – original draft, Methodology, Data curation. **Yangmao Wen:** Writing – original draft, Methodology, Data curation. **Xiaoran Wei:** Writing – original draft, Methodology, Data curation. **Neng Xiong:** Writing – original draft, Investigation, Data curation. **Xiong Xiong:** Writing – original draft, Funding acquisition, Conceptualization.

Declaration of competing interest

The authors declare that they have no known competing financial interests or personal relationships that could have appeared to influence the work reported in this paper.

Acknowledgments

We thank Prof. Hiroo Kanamori for his helpful discussion of the data-dependence of the finite-fault models, and we thank Prof. Aitaro Kato at the University of Tokyo for sharing relocated aftershocks following the 2023 Mj6.5 rupture. We thank Prof. Junichi Nakajima at the Department of Earth and Planetary Science, School of Science, Tokyo Institute of Technology for sharing three-dimensional seismic velocity structure along the Niigata-Kobe Tectonic Zone. Two anonymous reviewers provided helpful comments on the manuscript. C. Liu and X. Xiong were supported by the National Key R&D Program of China under grant 2022YFF0800703 and the National Natural Science Foundation of China (No. 42230309, 42222403). Y. B. was supported by the National Natural Science Foundation of China (No. 42376212). T. Lay's earthquake research is supported by US National Science Foundation (Grant EAR1802364). The Advanced Land Observation Satellite (ALOS)−2 data were provided by JAXA through the RA6 project (ID: ER3A2N040).

Supplementary materials

Supplementary material associated with this article can be found, in the online version, at doi:10.1016/j.epsl.2024.119107.

Data availability

Data will be made available on request.

References

Amezawa, Y., Hiramatsu, Y., Miyakawa, A., Imanishi, K., Otsubo, M., 2023. Long-living earthquake swarm and intermittent seismicity in the northeastern tip of the Noto Peninsula. Japan. Geophys. Res. Lett. 50, e2022GL102670.

Bai, Y., Cheung, K.F., 2013. Dispersion and nonlinearity of multi-layer non-hydrostatic free-surface flow. J Fluid Mech 726, 226–260.

Bai, Y., Yamazaki, Y., Cheung, K.F., 2018. Convergence of multilayer nonhydrostatic models in relation to Boussinesq-type equations. J. Waterway, Port, Coastal, and Ocean Eng. 144, 06018001-1.

Bai, Y., Liu, C., Lay, T., Cheung, K.F., Ye, L., 2022. Optimizing a model of coseismic rupture for the 22 July 2020 Mw 7.8 Simeonof earthquake by exploiting acute sensitivity of tsunami excitation across the shelf break. J. Geophys. Res. Solid Earth 127, e2022JB024484.

Bai, Y., Liu, C., Lay, T., Cheung, K.F., Yamazaki, Y., 2023. Fast and slow intraplate ruptures during the 19 October 2020 magnitude 7.6 Shumagin earthquake. Nat. Comm. 14, 2015.

Bedford, J., Moreno, M., Schurr, B., Bartsch, M., Oncken, O., 2015. Investigating the final seismic swarm before the Iquique-Pisagua 2014 Mw 8.1 by comparison of continuous GPS and seismic foreshock data. Geophys. Res. Lett. 42, 3820–3828.

Cebry, S.B.L., McLaskey, G.C., 2021. Seismic swarms produced by rapid fluid injection into a low permeability laboratory fault. Earth Planet Sci. Lett. 557, 116726.

Chen, A.C., Zebker, H.A., 2014. Reducing ionospheric effects in InSAR data using accurate coregistration. IEEE Trans. Geosci. Remote Sens. 52, 60–70.

Chen, X., Shearer, P.M., Abercrombie, R.E., 2012. Spatial migration of earthquakes within seismic clusters in Southern California: evidence for fluid diffusion. J. Geophys. Res. 117.

De Barros, L., Cappa, F., Deschamps, A., Dublanchet, P., 2020. Imbricated aseismic slip and fluid diffusion drive a seismic swarm in the Corinth Gulf, Greece. Geophys. Res. Lett. 47, e2020GL087142.

Dong, P., Xia, K., Xu, Y., Elsworth, D., Ampuero, J.P., 2023. Laboratory earthquakes decipher control and stability of rupture speeds. Nat. Comm. 14, 2427.

Dublanchet, P., De Barros, L., 2021. Dual seismic migration velocities in seismic swarms. Geophys. Res. Lett. 48, e2020GL090025.

Ellsworth, W.L., 2013. Injection-induced earthquakes. Science 341, 1225942.

Enescu, B., Hainzl, S., Ben-Zion, Y., 2009. Correlations of seismicity patterns in Southern California with surface heat flow data. Bull. Seism. Soc. Am. 99, 3114–3123.

Fujii, Y., Satake, K., 2024. Slip distribution of the 2024 Noto Peninsula earthquake (M_{JMA} 7.6) estimated from tsunami waveforms and GNSS data. Earth, Planets and Space 76, 44.

Gori, M., Rubino, V., Rosakis, A.J., Lapusta, N., 2021. Dynamic rupture initiation and propagation in a fluid-injection laboratory setup with diagnostics across multiple temporal scales. Proc. Nat. Acad. Sci. 118, e2023433118.

Hainzl, S., 2004. Seismicity patterns of earthquake swarms due to fluid intrusion and stress triggering. Geophys. J. Int. 159, 1090–1096.

Hauksson, E., et al., 2013. Report on the August 2012 Brawley earthquake swarm in Imperial Valley. Southern California. Seism. Res. Lett. 84, 177–189.

He, P., Wen, Y., Xu, C., Chen, Y., 2019. Complete three-dimensional near-field surface displacements from imaging geodesy techniques applied to the 2016 Kumamoto earthquake. Remote Sens. Environ. 232, 111321.

Holtkamp, S.G., Brudzinski, M.R., 2011. Earthquake swarms in circum-Pacific subduction zones. Earth Planet. Sci. Lett. 305, 215–225.

Horton, S., 2012. Disposal of hydrofracking waste fluid by injection into subsurface aquifers triggers earthquake swarm in central Arkansas with potential for damaging earthquake. Seism. Res. Lett. 83, 250–260.

Ishikawa, Y., Bai, L., 2024. The 2024 Mj7.6 Noto Peninsula, Japan earthquake caused by the fluid flow in the crust. Earthq. Res. Adv., 100292

Ishiyama, T., et al., 2017. Structures and active tectonics of compressionally reactivated back-arc failed rift across the Toyama trough in the Sea of Japan, revealed by multiscale seismic profiling. Tectonophys 710, 21–36.

Ji, C., Wald, D.J., Helmberger, D.V., 2002. Source description of the 1999 Hector Mine, California, earthquake, part I: wavelet domain inversion theory and resolution analysis. Bull. Seism. Soc. Am. 92, 1192–1207.

Ji, C., Helmberger, D.V., Wald, D.J., Ma, K.F., 2003. Slip history and dynamic implications of the 1999 Chi-Chi, Taiwan, earthquake. J. Geophys. Res. Solid Earth 108.

Kanamori, H., Anderson, D.L., 1975. Theoretical basis of some empirical relations in seismology. Bull. Seism. Soc. Am. 65, 1073–1095.

Kanamori, H., Ross, Z., Rivera, L., 2020. Estimation of radiated energy using the KiK-net downhole records—Old method for modern data. Geophys. J. Int. 221, 1029–1042.

Kato, A., et al., 2008. Three-dimensional velocity structure in the source region of the Noto Hanto Earthquake in 2007 imaged by a dense seismic observation. Earth Planets Space 60, 105–110.

Kato, A., et al., 2010. Variations of fluid pressure within the subducting oceanic crust and slow earthquakes. Geophys. Res. Lett. 37, L14310.

Kato, A., et al., 2011. Anomalous depth dependency of the stress field in the 2007 Noto Hanto, Japan, earthquake: potential involvement of a deep fluid reservoir. Geophys. Res. Lett. 38, L06306.

Kato, A., 2024. Implications of fault-valve behavior from immediate aftershocks following the 2023 Mj6.5 earthquake beneath the Noto Peninsula, central Japan. Geophys. Res. Lett. 51, e2023GL106444.

Kisslinger, C., 1975. Processes during the Matsushiro, Japan, earthquake swarm as revealed by leveling, gravity, and spring-flow observations. Geology 3, 57–62.

Kosuga, M., 2014. Seismic activity near the Moriyoshi-zan volcano in Akita Prefecture, northeastern Japan: implications for geofluid migration and a midcrustal geofluid reservoir. Earth Planets Space 66, 1–16.

Kurahashi, S., Masaki, K., Irikura, K., 2008. Source model of the 2007 Noto-Hanto earthquake (Mw 6.7) for estimating broad-band strong ground motion. Earth Planets Space 60, 89–94.

Li, L., Cheung, K.F., 2019. Numerical dispersion in non-hydrostatic modeling of long-wave propagation. Ocean Model 138, 68–87.

Liu, C., et al., 2023a. Complex multi-fault rupture and triggering during the 2023 earthquake doublet in southeastern Türkiye. Nat. Comm. 14, 5564.

Liu, C., Bai, Y., Lay, T., Feng, Y., Xiong, X., 2023b. Megathrust complexity and the up-dip extent of slip during the 2021 Chignik, Alaska Peninsula earthquake. Tectonophysics 854, 229808.

Liu, C., et al., 2015. Rupture process of the 2012 September 5 Mw 7.6 Nicoya, Costa Rica earthquake constrained by improved geodetic and seismological observations. Geophys. J. Int. 203, 175–183.

Lohman, R.B., McGuire, J.J., 2007. Earthquake swarms driven by aseismic creep in the Salton Trough. California. J. Geophys. Res. 112, B04405.

Marguin, V., Simpson, G., 2023. Influence of fluids on earthquakes based on numerical modeling. J. Geophys. Res.: Solid Earth 128, e2022JB025132.

Marsan, D., Reverso, T., Socquet, A., 2023. Earthquake swarms along the Chilean subduction zone, 2003–2020. Geophys. J. Int. 235, 2758–2777.

Ma, Z., Zeng, H., Luo, H., Liu, Z., Jiang, Y., Aoki …, Y., Wei, S., 2024. Slow rupture in a fluid-rich fault zone initiated the 2024 Mw 7.5 Noto earthquake. Science 385 (6711), 866–871.

Masuda, H., Sugawara, D., Cheng, A.C., Suppasri, A., Shigihara, Y., Kure, S., Imamura, F., 2024. Modeling the 2024 Noto Peninsula earthquake tsunami: implications for tsunami sources in the eastern margin of the Japan Sea. Geosci. Lett. 11 (1), 29.

Matsumoto, Y., Yoshida, K., Matsuzawa, T., Hasegawa, A., 2021. Fault-valve behavior estimated from intensive foreshocks and aftershocks of the 2017 M 5.3 Kagoshima Bay earthquake sequence, Kyushu, southern Japan. J. Geophys. Res.: Solid Earth 126, e2020JB020278.

Maurer, J., Dunham, E.M., Segall, P., 2020. Role of fluid injection on earthquake size in dynamic rupture simulations on rough faults. Geophys. Res. Lett. 47, e2020GL088377.

Miyazaki, K., Nakajima, J., Suenaga, N., Yoshioka, S., 2023. Deep subduction o the Philippine Sea slab and formation of slab window beneath central Japan. Earth, Planets and Space 75, 93.

Mogi, K., 1963. Some discussions on aftershocks, foreshocks and earthquake swarms-the fracture of a semi finite body caused by an inner stress origin and its relation to the earthquake phenomena. Bull. Earthq. Res. Inst. 41, 615–658.

Nakajima, J., 2022. Crustal structure beneath earthquake swarm in the Noto peninsula. Japan. Earth, Planets and Space 74, 160.

Nishimura, T., Hiramatsu, Y., Ohta, Y., 2023. Episodic transient deformation revealed by the analysis of multiple GNSS networks in the Noto Peninsula, central Japan. Sci Rep 13, 8381.

Normile, D., 2024. Mysterious seismic swarm foreshadowed monster Japan earthquake. Science 383, 140.

Okada, T., et al., 2015. Hypocenter migration and crustal seismic velocity distribution observed for the inland earthquake swarms induced by the 2011 Tohoku-Oki earthquake in NE Japan: implications for crustal fluid distribution and crustal permeability. Geofluids 15, 293–309.

Okada, Y., 1985. Surface deformation due to shear and tensile faults in a half-space. Bull. Seismol. Soc. Am. 75, 1135–1154.

Okuwaki, R., Yagi, Y., Murakami, A., Fukahata, Y., 2024. A multiplex rupture sequence under complex fault network due to preceding earthquake swarms during the 2024 Mw 7.5 Noto Peninsula, Japan, earthquake. Geophys. Res. Lett. 51, e2024GL109224.

Parsons, B., Wright, T., Rowe, P., Andrews, J., Jackson, J., Walker …, R., Engdahl, E.R., 2006. The 1994 Sefidabeh (eastern Iran) earthquakes revisited: new evidence from satellite radar interferometry and carbonate dating about the growth of an active fold above a blind thrust fault. Geophys. J. Int. 164, 202–217.

Passelégue, F.X., Almakari, M., Dublanchet, P., Barras, F., Fortin, J., Violay, M., 2020. Initial effective stress controls the nature of earthquakes. Nat. Comm. 11, 5132.

Passelégue, F.X., Brantut, N., Mitchell, T.M., 2018. Fault reactivation by fluid injection: controls from stress state and injection rate. Geophys. Res. Lett. 45, 12837–12846.

Rice, J.R., 1992. Fault stress states, pore pressure distributions, and the weakness of the San Andreas fault. Int. Geophys. 51, 475–503.

Ross, Z.E., Cochran, E.S., 2021. Evidence for latent crustal fluid injection transients in Southern California from long-duration earthquake swarms. Geophys. Res. Lett. 48, e2021GL092465.

Ross, Z.E., Rollins, C., Cochran, E.S., Hauksson, E., Avouac, J.P., Ben-Zion, Y., 2017. Aftershocks driven by afterslip and fluid pressure sweeping through a fault-fracture mesh. Geophys. Res. Lett. 44, 8260–8267.

Shelly, D.R., 2024. Examining the connections between earthquake swarms, crustal fluids, and large earthquakes in the context of the 2020-2024 Noto Peninsula, Japan, earthquake sequence. Geophys. Res. Lett. 51, e2023GL107897.

Shelly, D.R., Hill, D.P., Massin, F., Farrell, J., Smith, R.B., Taira, T.A., 2013. A fluid-driven earthquake swarm on the margin of the Yellowstone caldera. J. Geophys. Res.: Solid Earth 118, 4872–4886.

Shelly, D.R., Ellsworth, W.L., Hill, D.P., 2016. Fluid-faulting evolution in high definition: connecting fault structure and frequency-magnitude variations during the 2014 Long Valley Caldera, California, earthquake swarm. J. Geophys. Res.: Solid Earth 121, 1776–1795.

Tanioka, Y., Satake, K., 1996. Tsunami generation by horizontal displacement of ocean bottom. Geophys. Res. Lett. 23, 861–864.

Umeda, K., Ninomiya, A., Negi, T., 2009. Heat source for an amagmatic hydrothermal system, Noto Peninsula, Central Japan. J. Geophys. Res. 114, B01202.

Vidale, J.E., Boyle, K.L., Shearer, P.M., 2006. Crustal earthquake bursts in California and Japan: their patterns and relation to volcanoes. Geophys. Res. Lett. 33, L20313.

Wang, R., Schurr, B., Milkereit, C., Shao, Z., Jin, M., 2011. An improved automatic scheme for empirical baseline correction of digital strong-motion records. Bull. Seismol. Soc. Am. 101, 2029–2044.

Wei, X., Zhi, H., Bai, Y., 2024. Multi-layer non-hydrostatic free-surface flow model with kinematic seafloor for seismic tsunami generation. Coastal Engineering 193, 104580.

Wegnüller, U., et al., 2016. Sentinel-1 support in the GAMMA software. Proc. Comput. Sci. 100, 1305–1312.

Xu, L., Ji, C., Meng, L., Ampuero, J.P., Yunjun, Z., Mohanna, S., Aoki, Y., 2024. Dual-initiation ruptures in the 2024 Noto earthquake encircling a fault asperity at a swarm edge. Science 385 (6711), 871–876.

Yamanaka, Y., Matsuba, Y., Shimozono, T., Tajima, Y., 2024. Nearshore propagation and amplification of the tsunami following the 2024 Noto Peninsula earthquake, Japan. Geophys. Res. Lett. in press.

Yamashita, T., 1999. Pore creation due to fault slip in a fluid-permeated fault zone and its effect on seismicity: generation mechanism of earthquake swarm. Pure Appl. Geophys. 155, 625–647.

Yamazaki, Y., Kowalik, Z., Cheung, K.F., 2009. Depth-integrated, non-hydrostatic model for wave breaking and run-up. Internat. J. Numer. Methods Fluids 61, 473–497.

Yamazaki, Y., Cheung, K.F., Kowalik, Z., 2011. Depth-integrated, non-hydrostatic model with grid nesting for tsunami generation, propagation, and run-up. Internat. J. Numer. Methods Fluids 67, 2081–2107.

Yang, S., Sang, C., Hu, Y., Wang, K., 2024. Coseismic and early postseismic deformation of the 2024 Mw7. 45 Noto Peninsula earthquake. Geophys. Res. Lett. 51 (11), e2024GL108843.

Ye, L., Lay, T., Kanamori, H., Rivera, L., 2016. Rupture characteristics of major and great (Mw $\geq$ 7.0) megthrust earthquakes from 1990 to 2015: 1. Source parameter scaling relationships. J. Geophys. Res.: Solid Earth 121, 826–844.

Yoshida, K., Saito, T., Urata, Y., Asano, Y., Hasegawa, A., 2017. Temporal changes in stress drop, frictional strength, and earthquake size distribution in the 2011 Yamagata-Fukushima, NE Japan, earthquake swarm, caused by fluid migration. J. Geophys. Res.: Solid Earth 122, 10–379.

Yoshida, K., Hasegawa, A., 2018. Sendai-Okura earthquake swarm induced by the 2011 Tohoku-Oki earthquake in the stress shadow of NE Japan: detailed fault structure and hypocenter migration. Tectonophys 733, 132–147.

Yoshida, K., et al., 2023a. Upward earthquake swarm migration in the northeastern Noto Peninsula, Japan, initiated from a deep ring-shaped cluster: possibility of fluid leakage from a hidden magma system. J. Geophys. Res.: Solid Earth 128 (2023), e2022JB026047.

Yoshida, K., et al., 2023b. Updip fluid flow in the crust of the northeastern Noto Peninsula, Japan, triggered the 2023 Mw 6.2 Suzu earthquake during swarm activity. Geophys. Res. Lett. 50, e2023GL106023.

Yoshimura, R., et al., 2008. Magnetotelluric observations around the focal region of the 2007 Noto Hanto Earthquake (Mj 6.9), Central Japan. Earth Planets Space 60, 117–122.

Yukutake, Y., Ito, H., Honda, R., Harada, M., Tanada, T., Yoshida, A., 2011. Fluid-induced swarm earthquake sequence revealed by precisely determined hypocenters and focal mechanisms in the 2009 activity at Hakone volcano, Japan. J. Geophys. Res. 116, B04308.

Supplementary Materials for

Shallow crustal rupture in a major M_W 7.5 earthquake above a deep crustal seismic swarm along the Noto Peninsula in western Japan

Chengli Liu[1*], Yefei Bai[2, 3*], Thorne Lay[4], Ping He[1], Yangmao Wen[5], Xiaoran Wei[2], Neng Xiong[6] & Xiong Xiong[1]

[1]Hubei Subsurface Multi-Scale Imaging Key Laboratory, School of Geophysics and Geomatics, China University of Geosciences, Wuhan, China.
[2]Ocean College, Zhejiang University, Zhoushan, Zhejiang, 316021, China.
[3]Hainan Institute, Zhejiang University, Sanya, Hainan, 572024, China.
[4]Department of Earth and Planetary Sciences, University of California Santa Cruz, Santa Cruz, CA, USA.
[5]School of Geodesy and Geomatics, Wuhan University, Wuhan, China.
[6]Department of Earth, Environmental, and Planetary Sciences, Rice University, Houston, TX, USA.

*Corresponding author: Chengli Liu: liuchengli@cug.edu.cn and Yefei Bai: yfbai@zju.edu.cn

This file includes:

Figs. S1 to S18
Tables S1 to S2

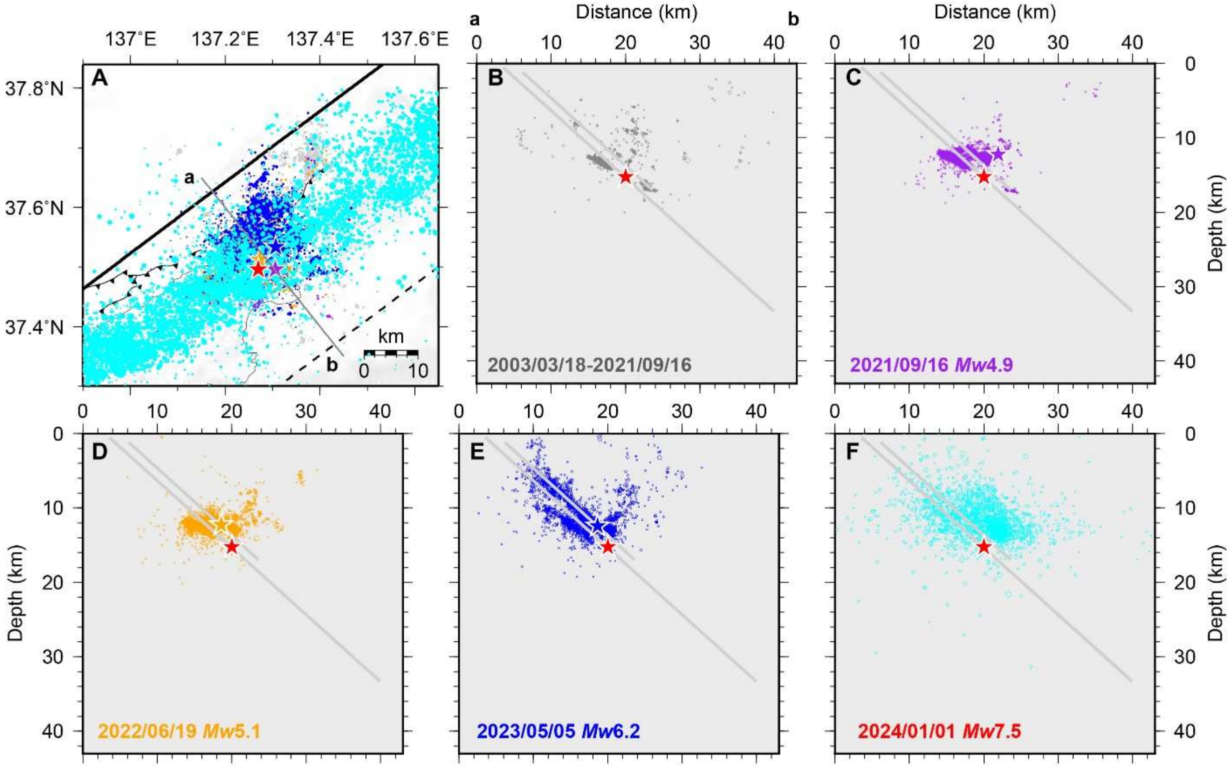

Fig. S1. Map and cross-sections depicting the distribution of seismic swarm and shallower crustal activity along the northeast Noto Peninsula. (A), The swarm region as highlighted in Figure 1A, showing the relocated catalog from 2003/03/08 to 2023/07/10 (*28*) and JMA activity from 2024/01/01 to 2024/02/01. Stars indicate hypocenters of larger earthquakes. (B), Depth distribution of seismic activity along profile AB (marked in A) preceding the M_W 4.9 event on September 16, 2021. Swarm activity is located from 10 to 18 km deep. Later time intervals are shown in (C)-(E) with magenta, orange, and blue circles, sized proportionally to magnitude, denoting relocated aftershocks with magnitudes greater than 1.0, or each of the larger events (colored stars) at the start of labeled time intervals. The red stars denote the mainshock hypocenter. (F), Cyan circles indicate the 1-month aftershocks of the 2024 mainshock event from the JMA catalog. Gray lines in (B)-(F) represent the fault position and dip direction for the 2023 M_W 6.2 event (depicted with a short line) and the 2024 M_W 7.5 event (depicted with a long line).

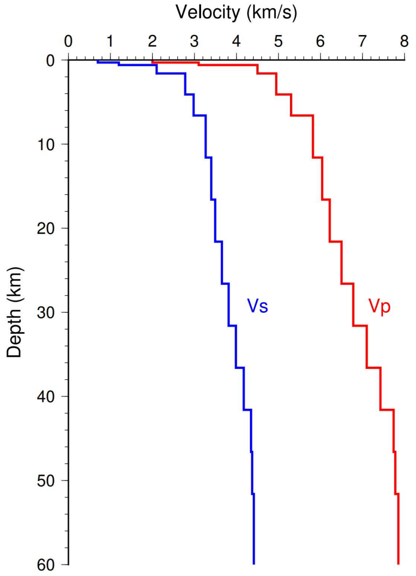

Fig. S2. The 1D velocity model was used in this study.

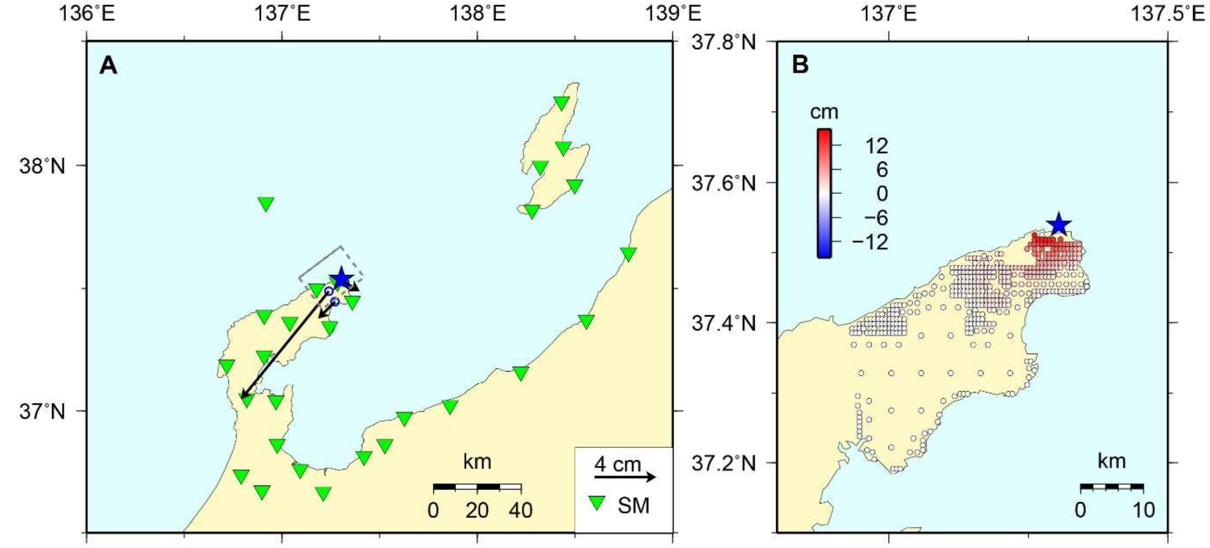

Fig. S3. Near-field data used in the finite-fault inversion for the 2023 M_W 6.2 earthquake. (A), Green inverted triangles indicate the location of strong-motion stations, and black vectors indicate coseismic GPS horizontal displacements. The blue star is the epicenter of the 2023 M_W 6.2 event. (B), The down-sampled unwrapped InSAR LOS displacements.

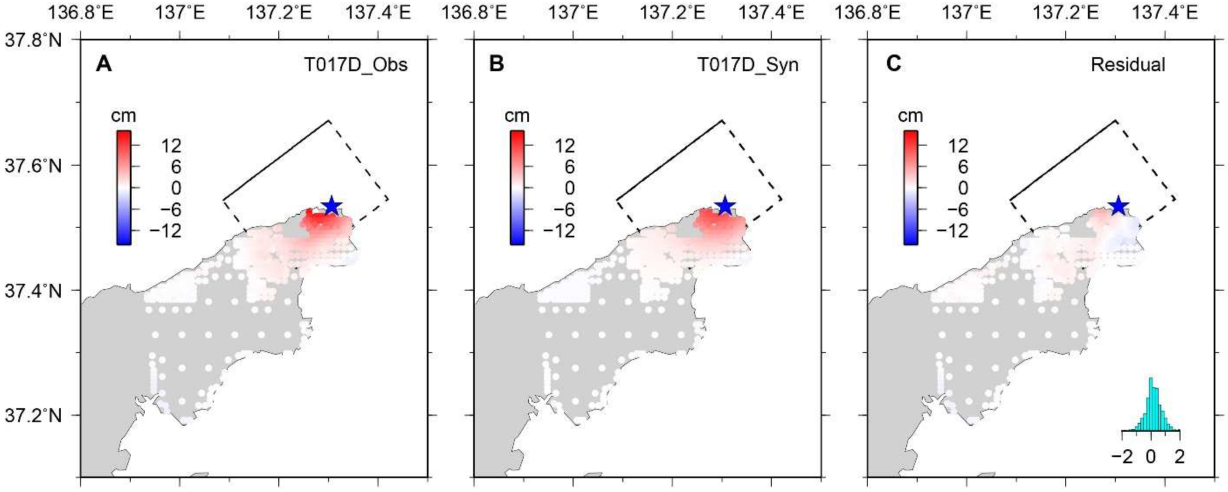

Fig. S4. InSAR fits for the finite-fault joint inversion model of the 2023 M_W 6.2 event shown in Figure 4. (A), (B), and (C) show the observed, prediction, and residuals of the InSAR LOS displacements, respectively.

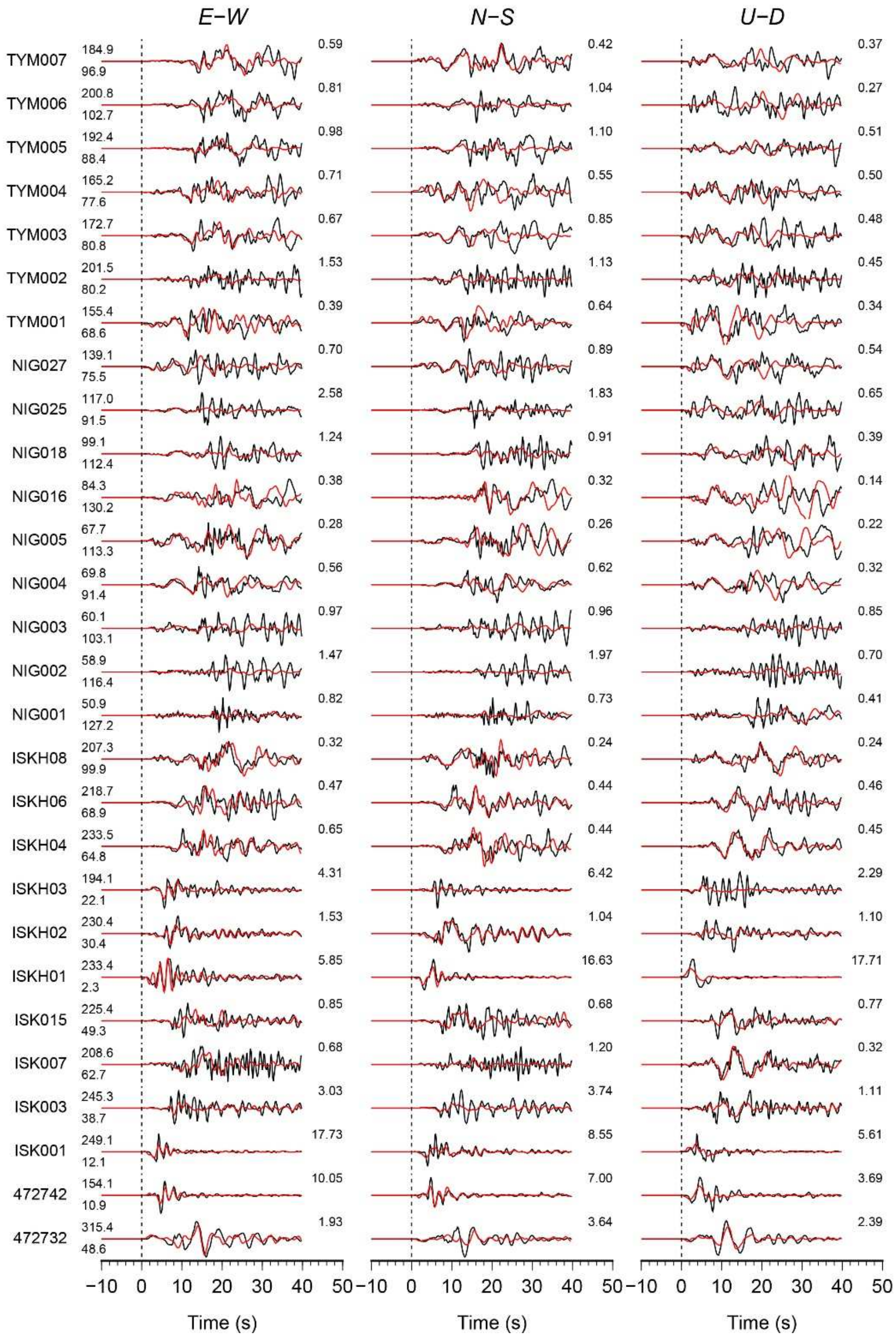

Fig. S5. Three-component strong-motion ground velocity fits for the finite-fault joint inversion model of the 2023 M_W 6.2 earthquake in Figure 4. Data (black) and synthetics (red) are aligned on the first P arrivals. The station name is listed on the left of each row. The azimuth (above) and epicentral distance (below) in degrees are shown at the beginning of each record. The numbers at the upper right of each waveform comparison indicate the maximum observed ground velocity in cm/s.

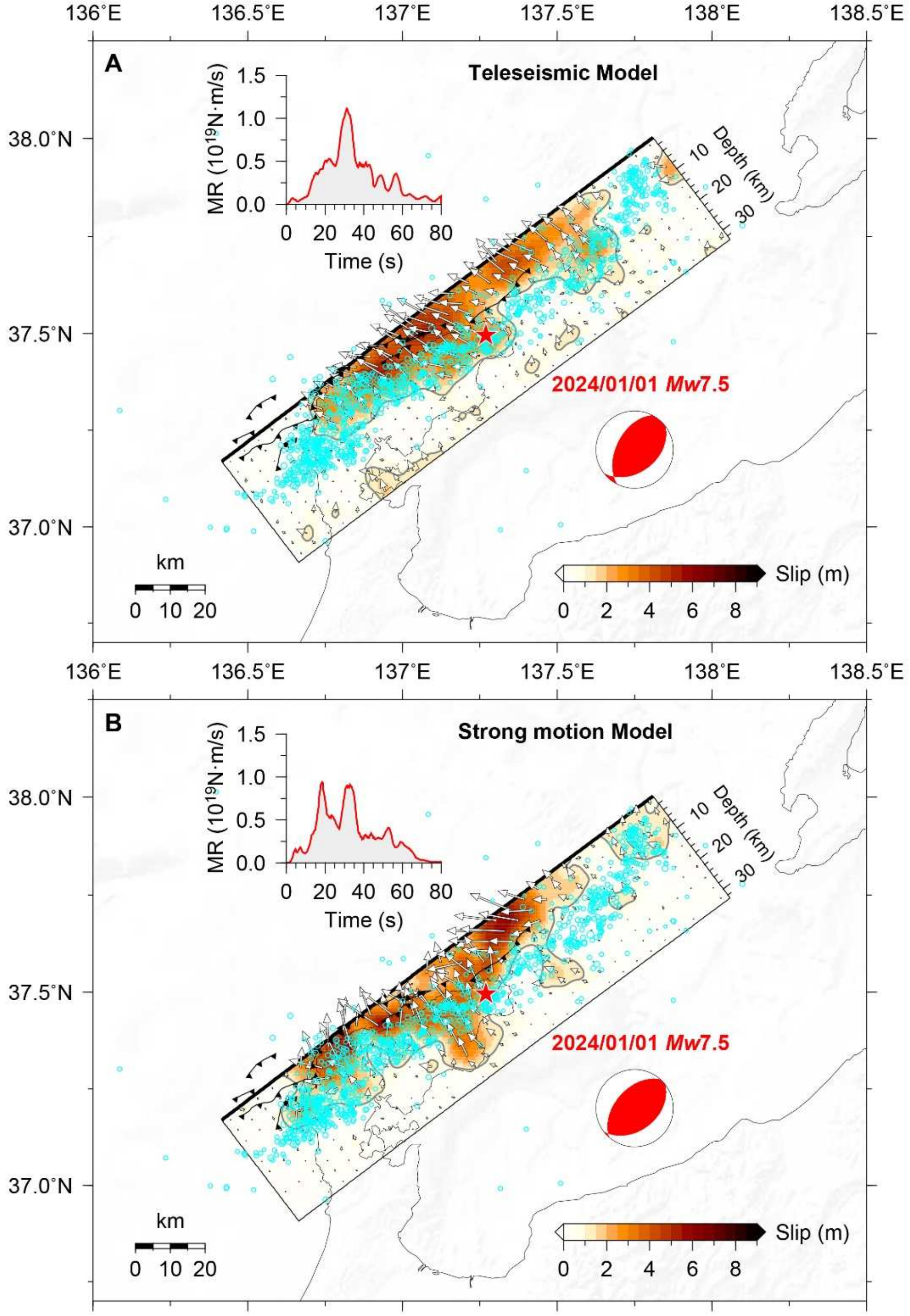

Fig. S6. Finite-fault models from separate seismic data sets for the 2024 M_W 7.5 earthquake. (A), The slip model inverted using only teleseismic P and SH wave data. (B), The slip model inverted using only strong-motion data. Gray contours in each model highlight the 1 m slip contour, and white arrows indicate the direction of the slip. The cyan circles represent 1-month aftershocks with a magnitude of $M \geqslant 3.0$ from the JMA catalog. The red focal mechanism is the moment tensor derived from the slip model. Black barbed lines represent active faults. The insets show the moment-rate functions (MRF) of each seismic model.

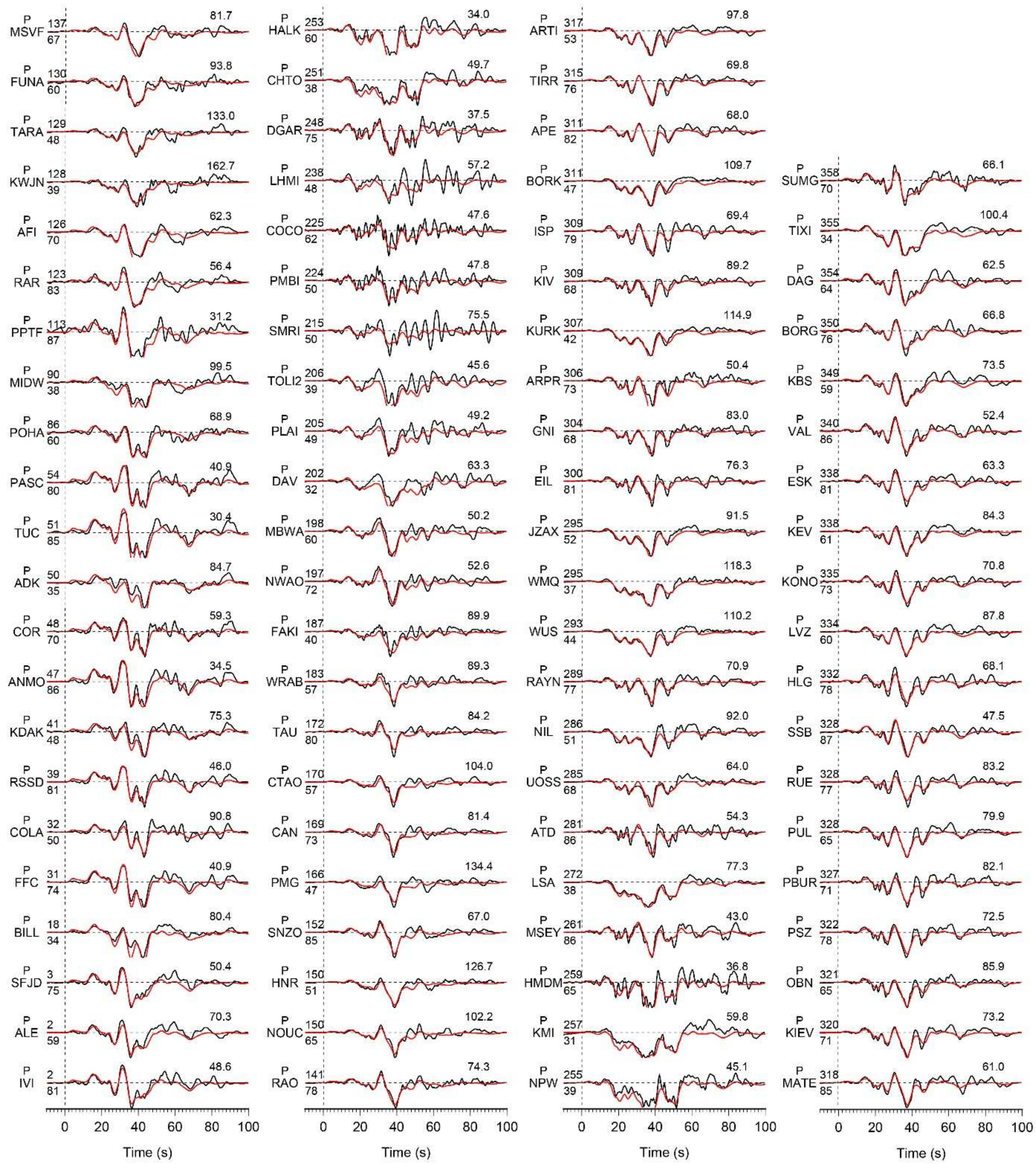

Fig. S7A. Comparison of observed (black) and synthetic (red) teleseismic *P*-wave ground displacements for the teleseismic-based model shown in Figure S6A. Data and synthetic seismograms are manually aligned on the first arrivals. Station names and phase types are indicated on the left of each comparison. The azimuth (above) and epicentral distance (below) in degrees are shown at the beginning of each record. The number above the right portion of each comparison is the peak amplitude of the observed ground displacement in μm.

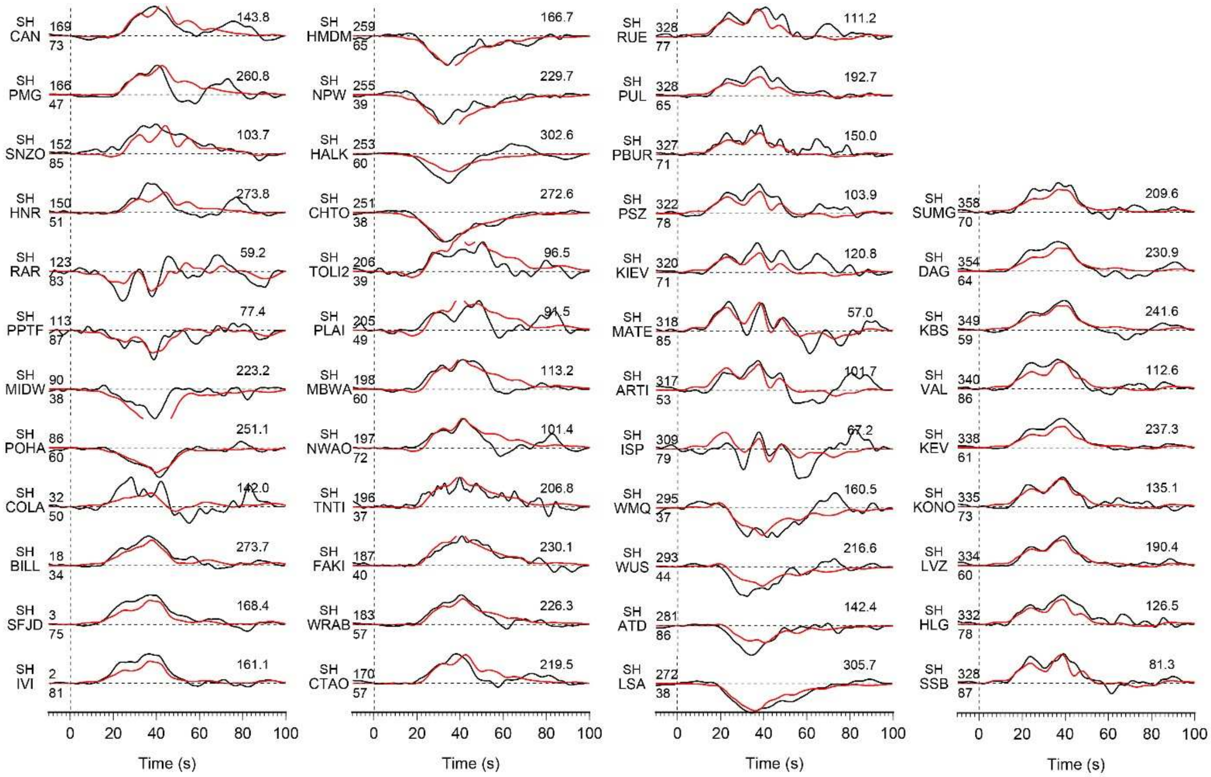

Fig. S7B. The same as figure S7A, but for *SH*-waves.

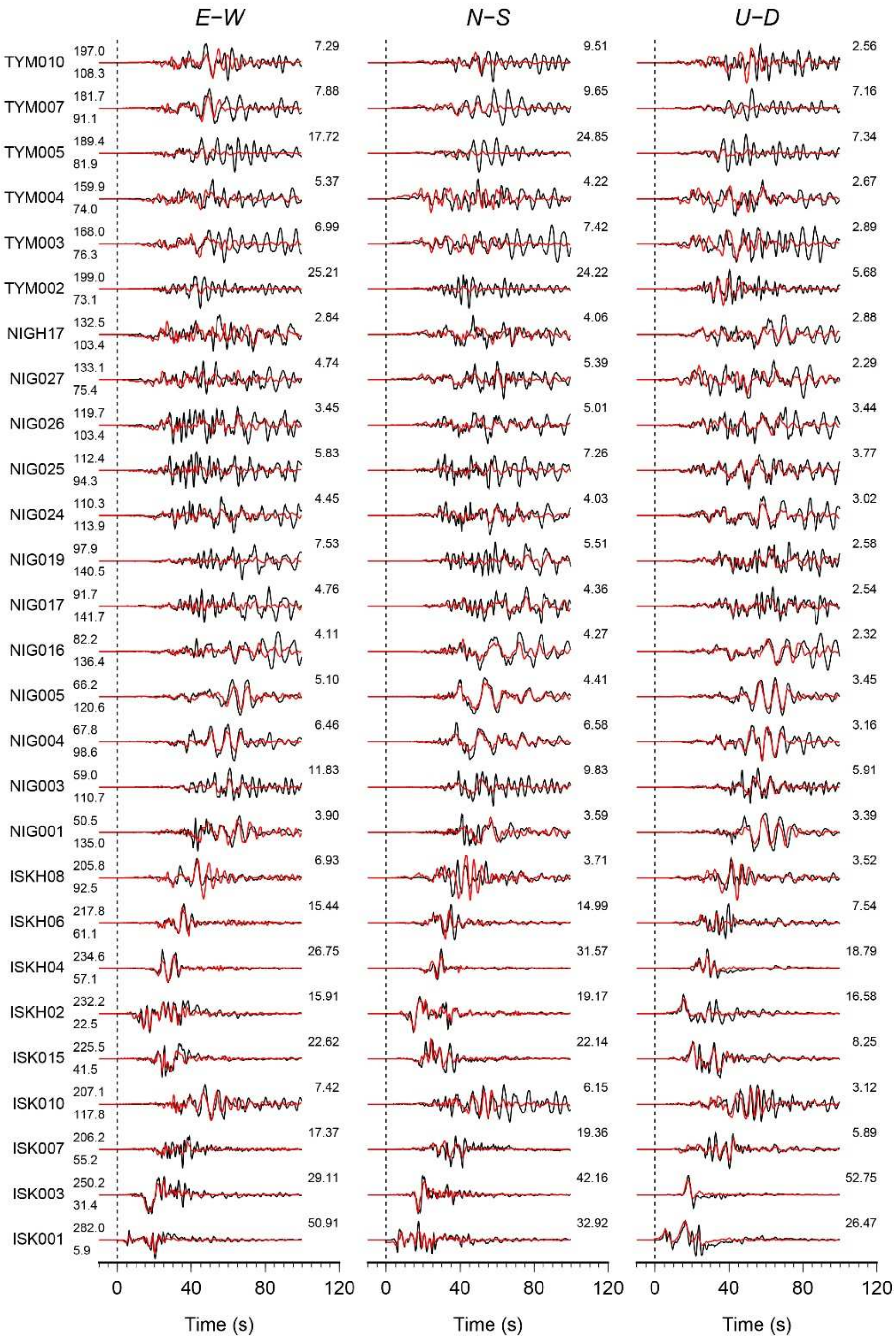

Fig. S8. Comparisons of three-component strong motion ground velocity observations (black) and synthetic seismograms (red) for the strong-motion-based model shown in Figure S6B. Data and synthetics are aligned on the first P arrivals. The station name is listed on the left of each row. The azimuth (above) and epicentral distance (below) in degrees are shown at the beginning of each record. The numbers at the upper right of each waveform comparison indicate the maximum observed ground velocity in cm/s.

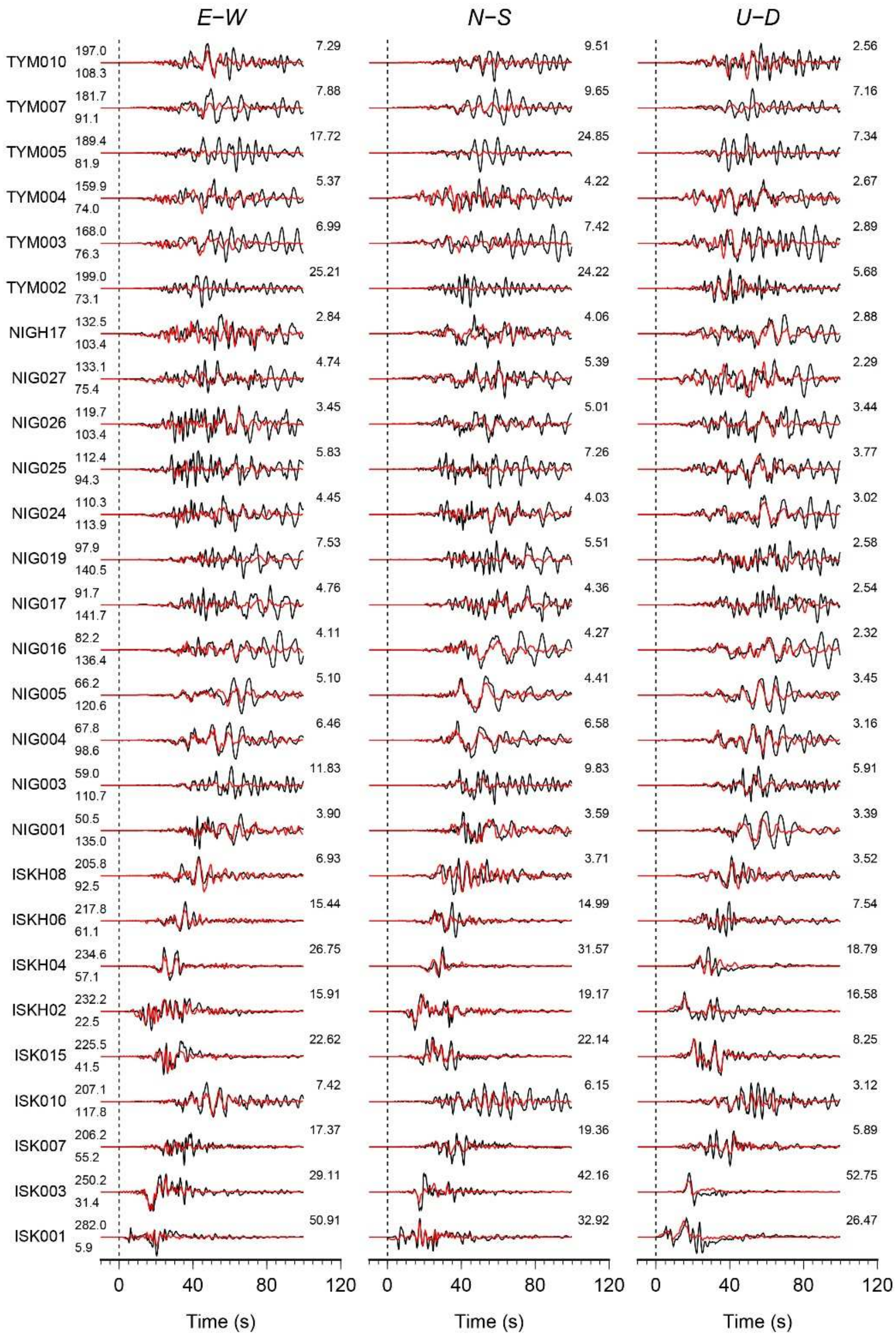

Fig. S9. Comparisons of three-component strong motion ground velocity observations (black) and synthetic seismograms (red) for the joint seismic model shown in Figure 5A. Data and synthetics are aligned on the first P arrivals. The station name is listed on the left of each row. The azimuth (above) and epicentral distance (below) in degrees are shown at the beginning of each record. The numbers at the upper right of each waveform comparison indicate the maximum observed ground velocity in cm/s.

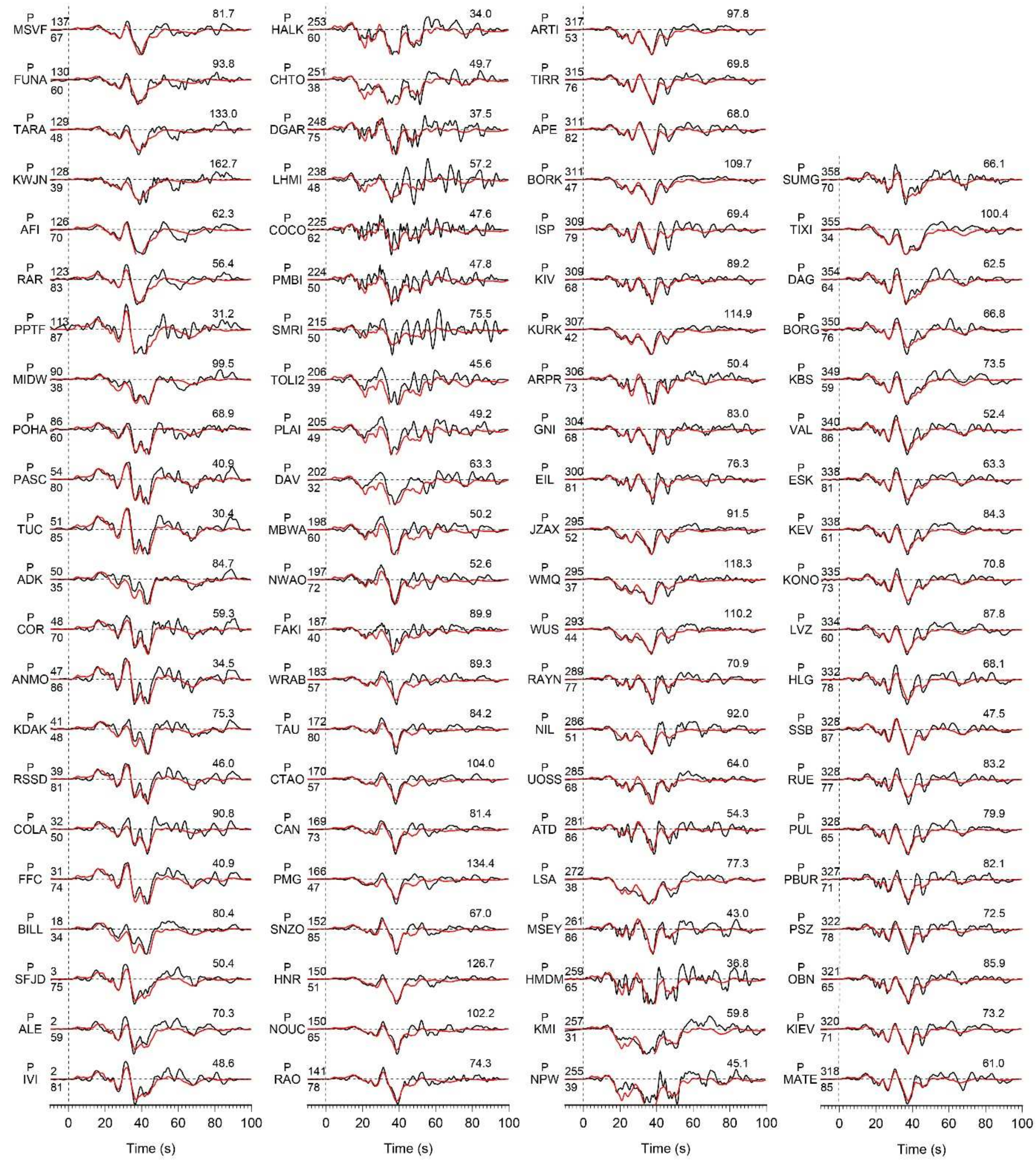

Fig. S10A. Comparison of observed (black) and synthetic (red) teleseismic *P*-wave ground displacements for the joint seismic model shown in Figure 5A. Data and synthetic seismograms are manually aligned on the first arrivals. Station names and phase types are indicated on the left of each comparison. The azimuth (above) and epicentral distance (below) in degrees are shown at the beginning of each record. The number above the right portion of each comparison is the peak amplitude of the observed ground displacement in μm.

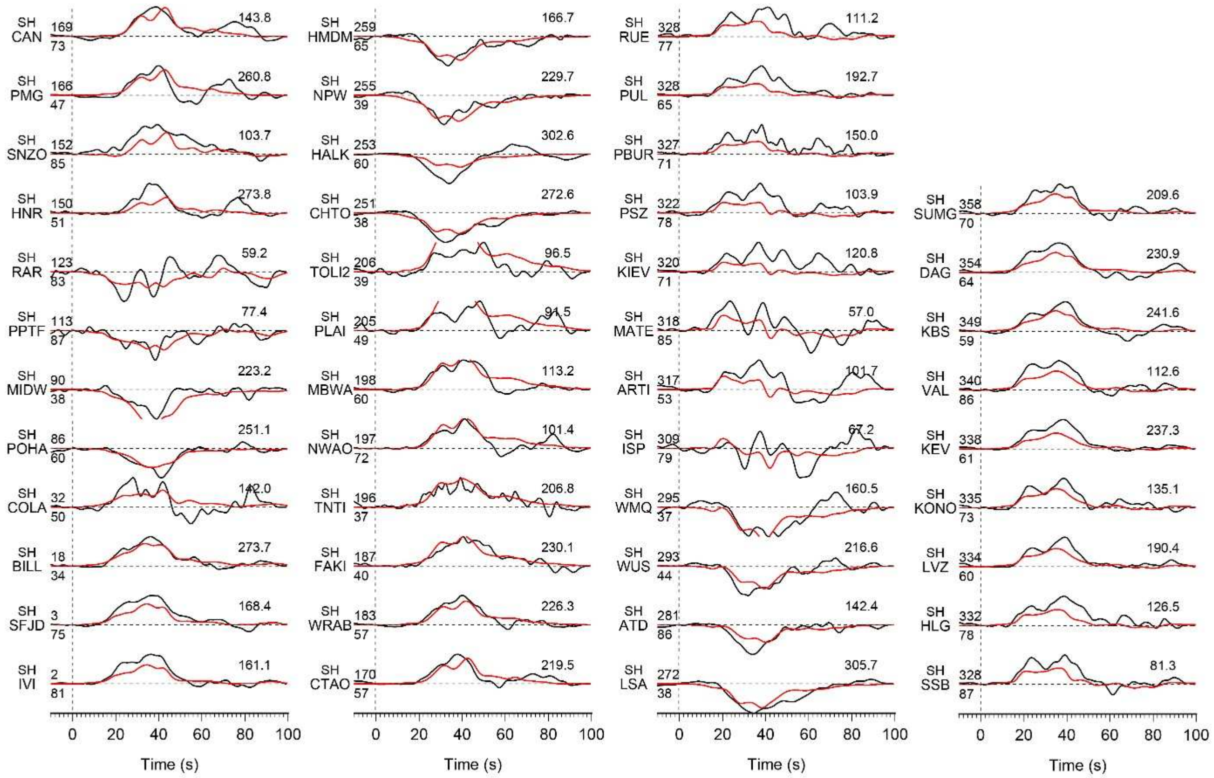

Fig. S10B. The same as figure S10A, but for *SH*-waves.

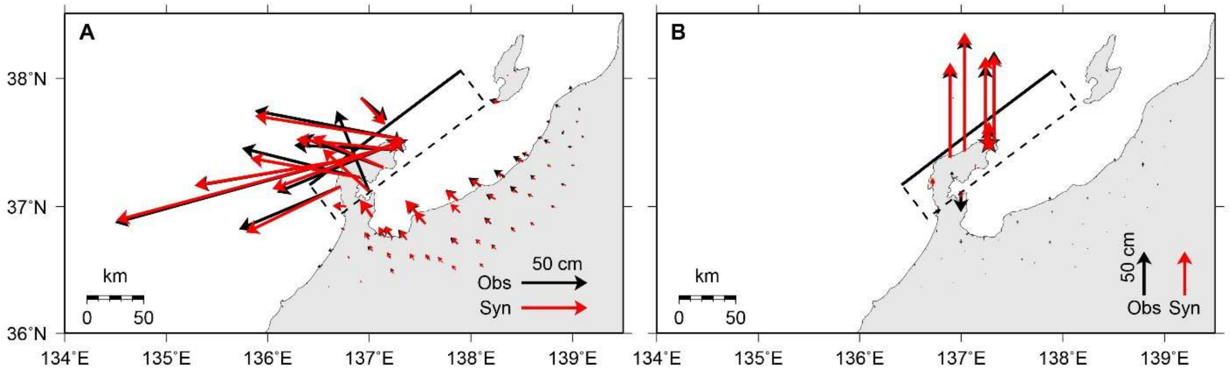

Fig. S11A. GPS fitting for the static model of the 2024 M_W 7.5 event shown in Figure 5B. (A), The horizontal GPS displacements with observed data in black and synthetic data in red. (B), The vertical GPS displacements are shown in black, with synthetic data in red. The black dashed rectangle indicates the assumed fault model, with a solid line depicting the shallow edge.

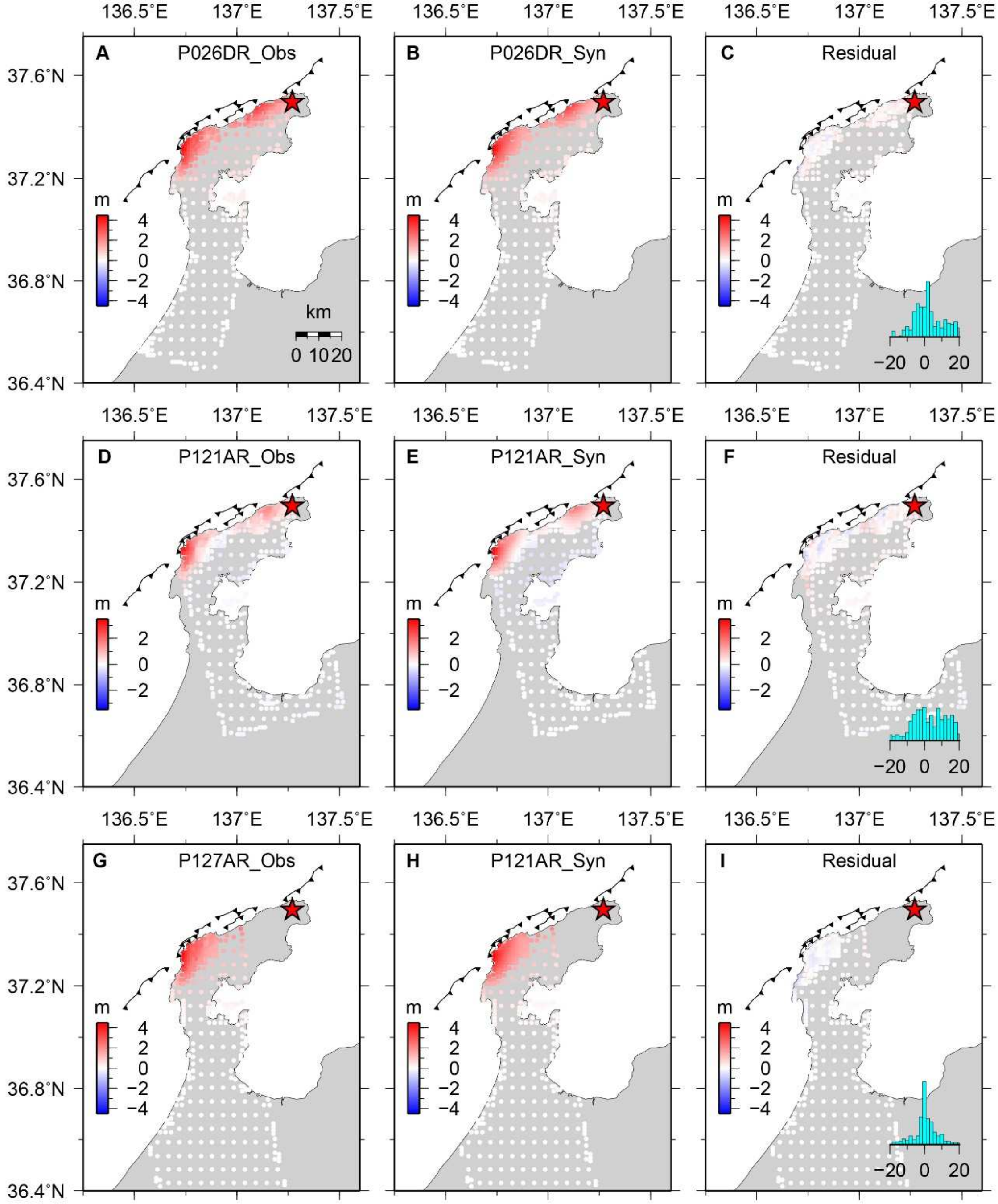

Fig. S11B. InSAR range offset fitting for the static model of the 2024 M_W 7.5 earthquake shown in Figure 5B. (A), (D), and (G), show the range offset of the descending track P026, ascending tracks P121 and P127, respectively. (B), (E), and (H), indicate the prediction of range offsets derived from the static slip model. (C), (F), and (I), represent residuals of range offsets along the ascending and descending paths, respectively. The active faults are denoted by black barbed lines, with the epicenter of the 2024 M_W 7.5 earthquake marked by a red star.

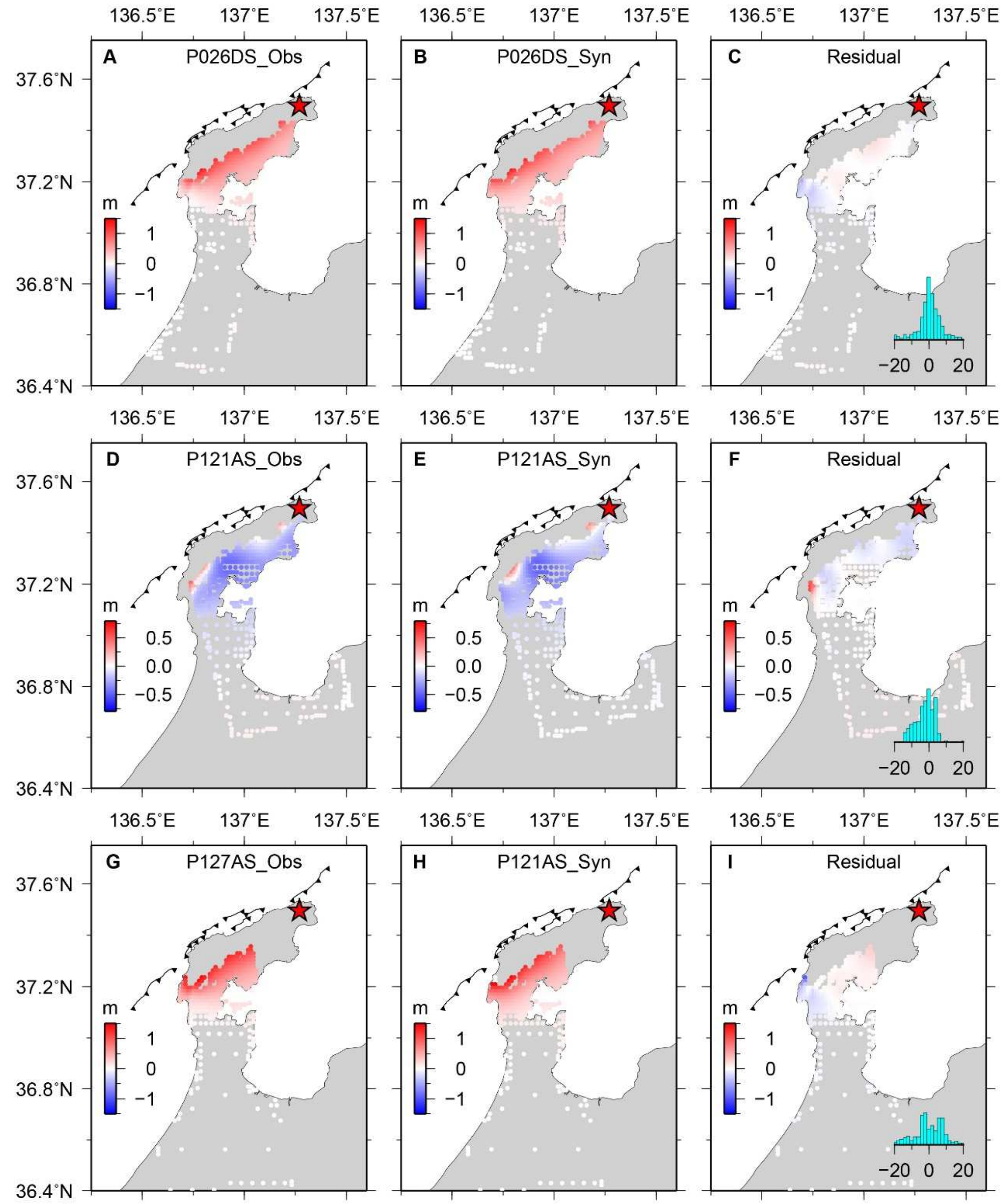

Fig. S11C. The same as Figure S11B, but for the InSAR LOS displacements.

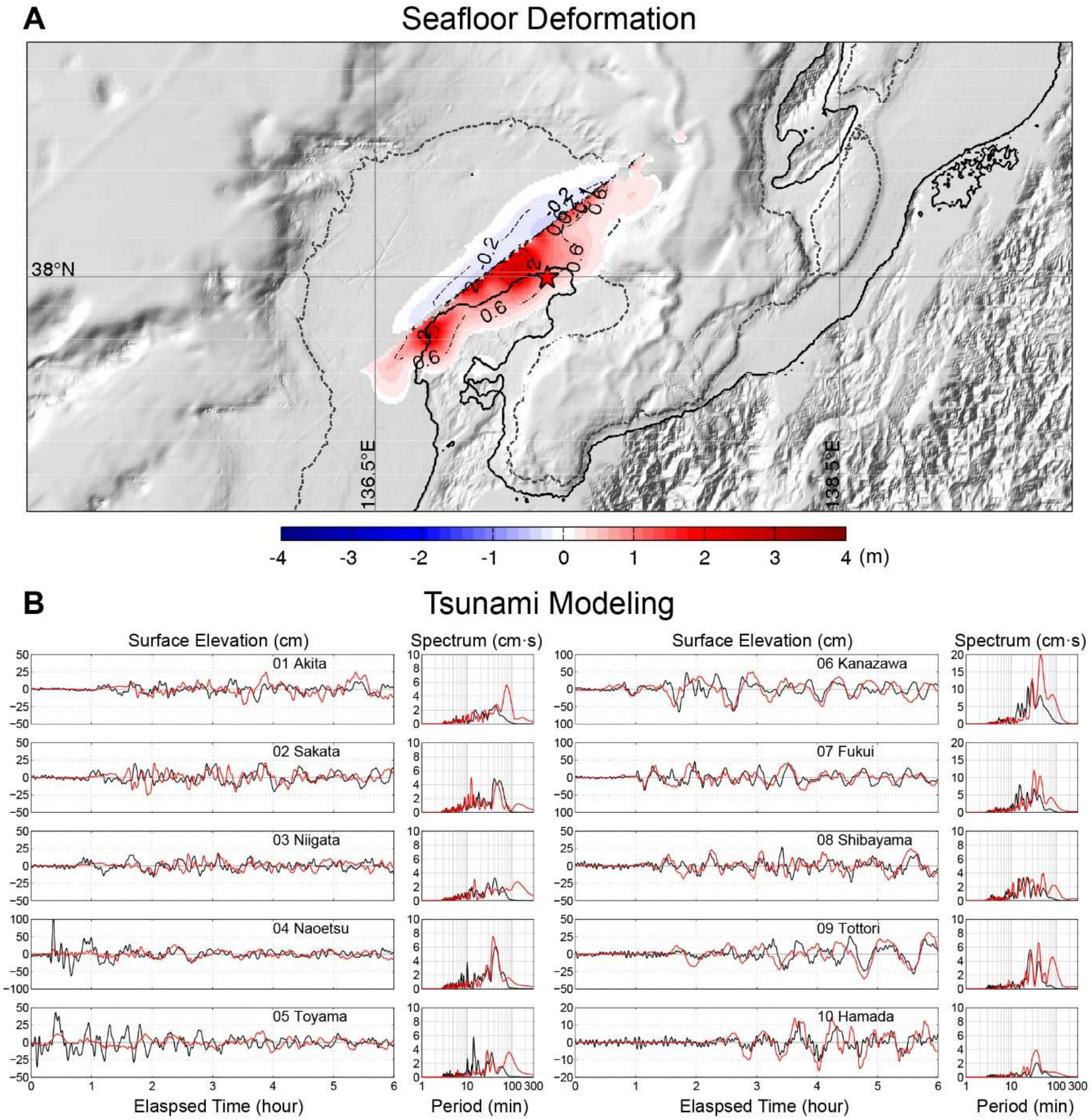

Fig. S12. Tsunami predictions for the joint seismic model in Figure 5A. (A), Vertical seafloor and land surface deformation computed for the joint seismic model. (B), Comparison of tsunami waveforms and predictions at the seafloor pressure stations shown in Figure 2A. Black lines represent observed time series (left) and amplitude spectra (right), while red lines indicate the predictions.

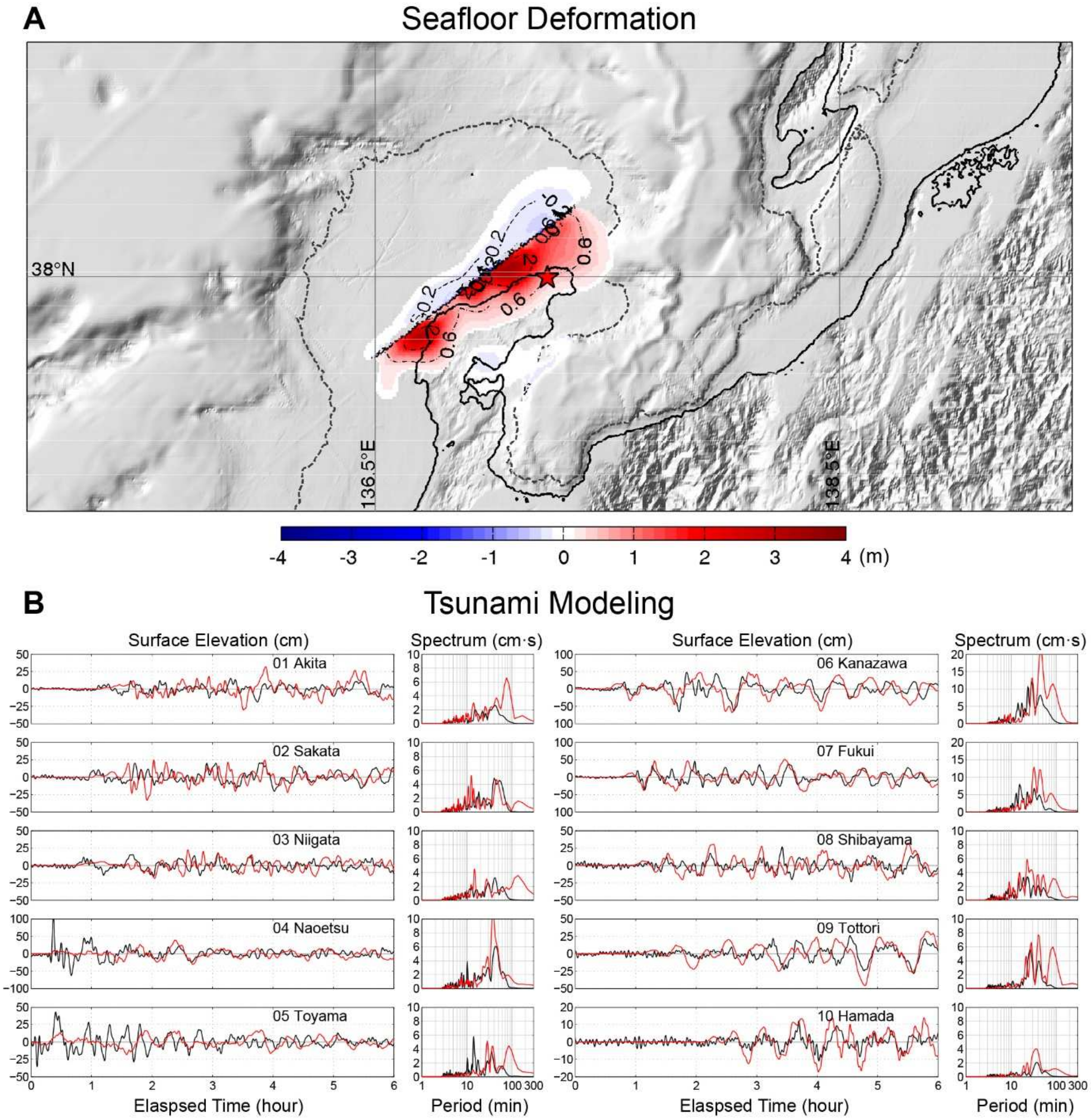

Fig. S13. Tsunami predictions for the joint static model in Figure 5B. (A), Vertical seafloor and land surface deformation computed for the joint static model. (B), Comparison of tsunami waveforms and predictions at the seafloor pressure stations shown in Figure 2A. Black lines represent observed time series (left) and amplitude spectra (right), while red lines indicate the predictions.

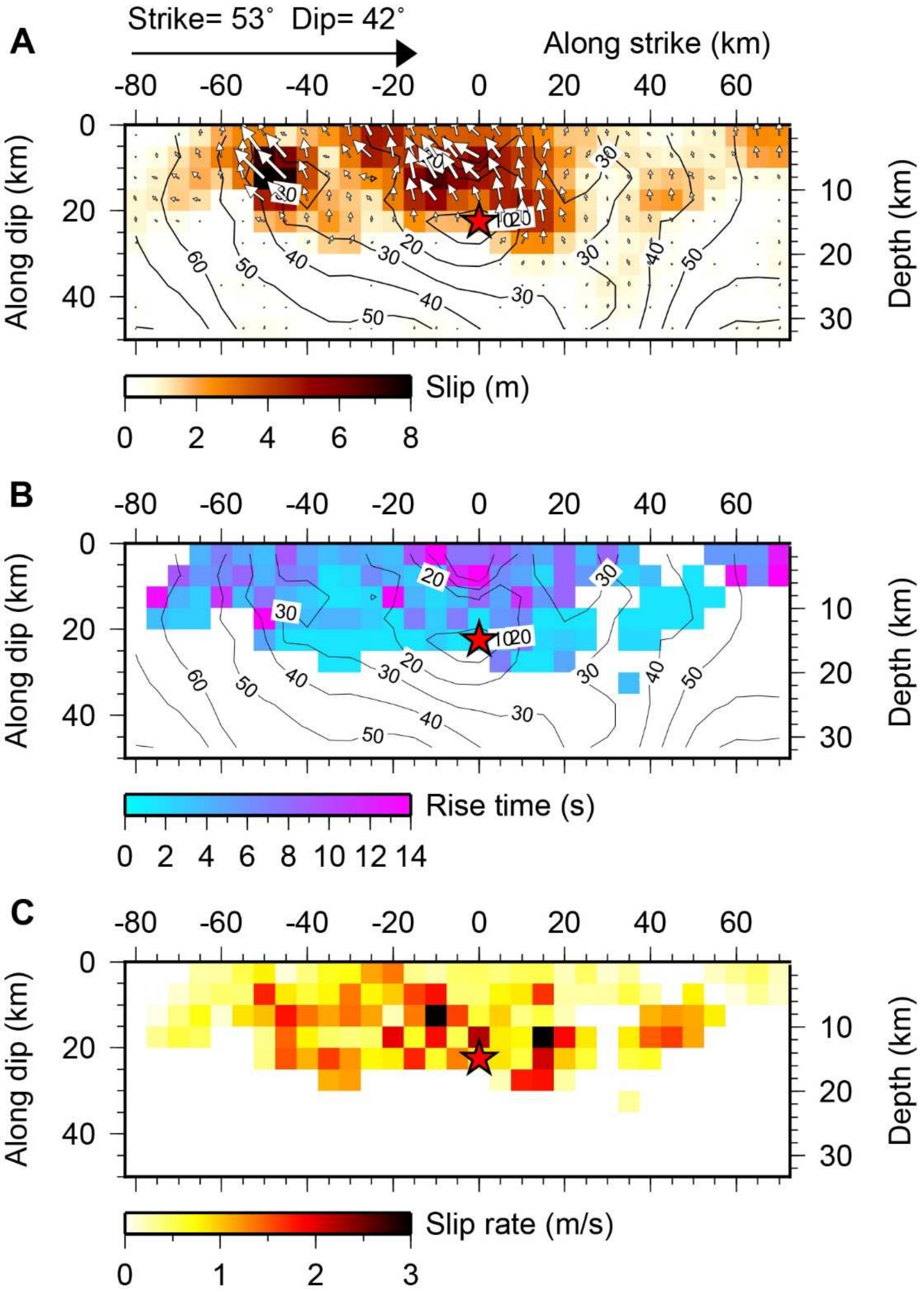

Fig. S14. Details of the preferred slip model for the 2024 M_W 7.5 earthquake. (A), The inverted slip distribution. The red star indicates the hypocenter. Black contours indicate the position of rupture initiation time in seconds. White arrows illustrate the variable direction of slip. The color bar indicates the scale for slip amplitude. (B) and (C), represent the distribution of rise time and slip rate of the preferred slip model, respectively. Subfaults with slip magnitudes less than 1 m are excluded. The slip rate is the ratio of fault slip to rise time.

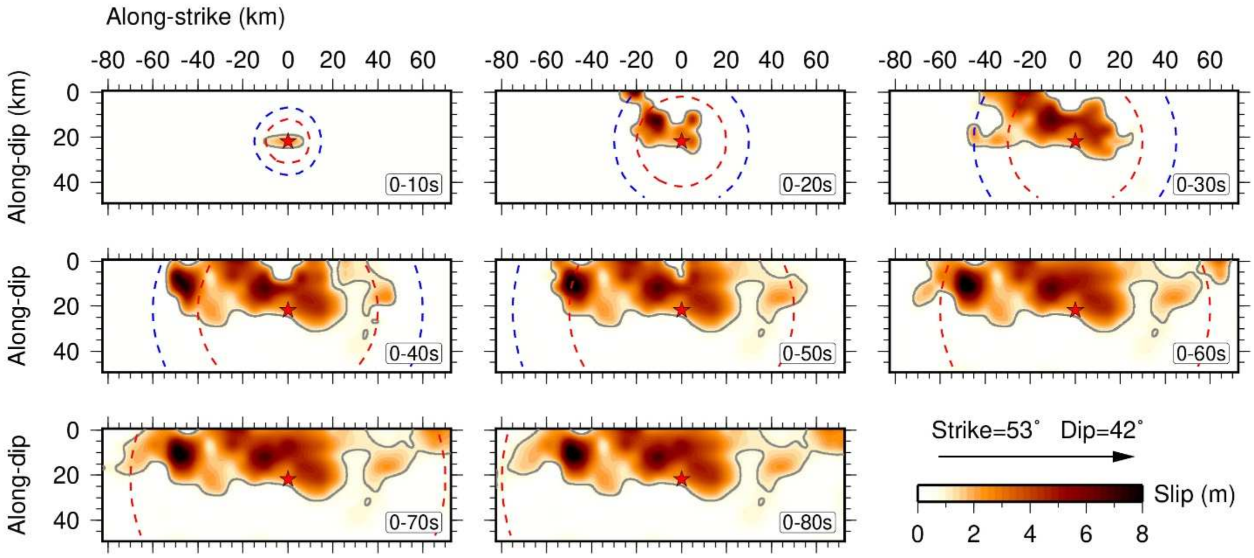

Fig. S15. Rupture snapshots for the preferred slip model shown in Figure 6 and Figure 13A, with a time step of 10 s. The color indicates the fault slip, while the red and blue dashed contours denote the pseudo-rupture front for rupture velocities of 1.0 and 1.5 km/s, respectively. Gray contours highlight the region with slip $\geqslant 1$ m.

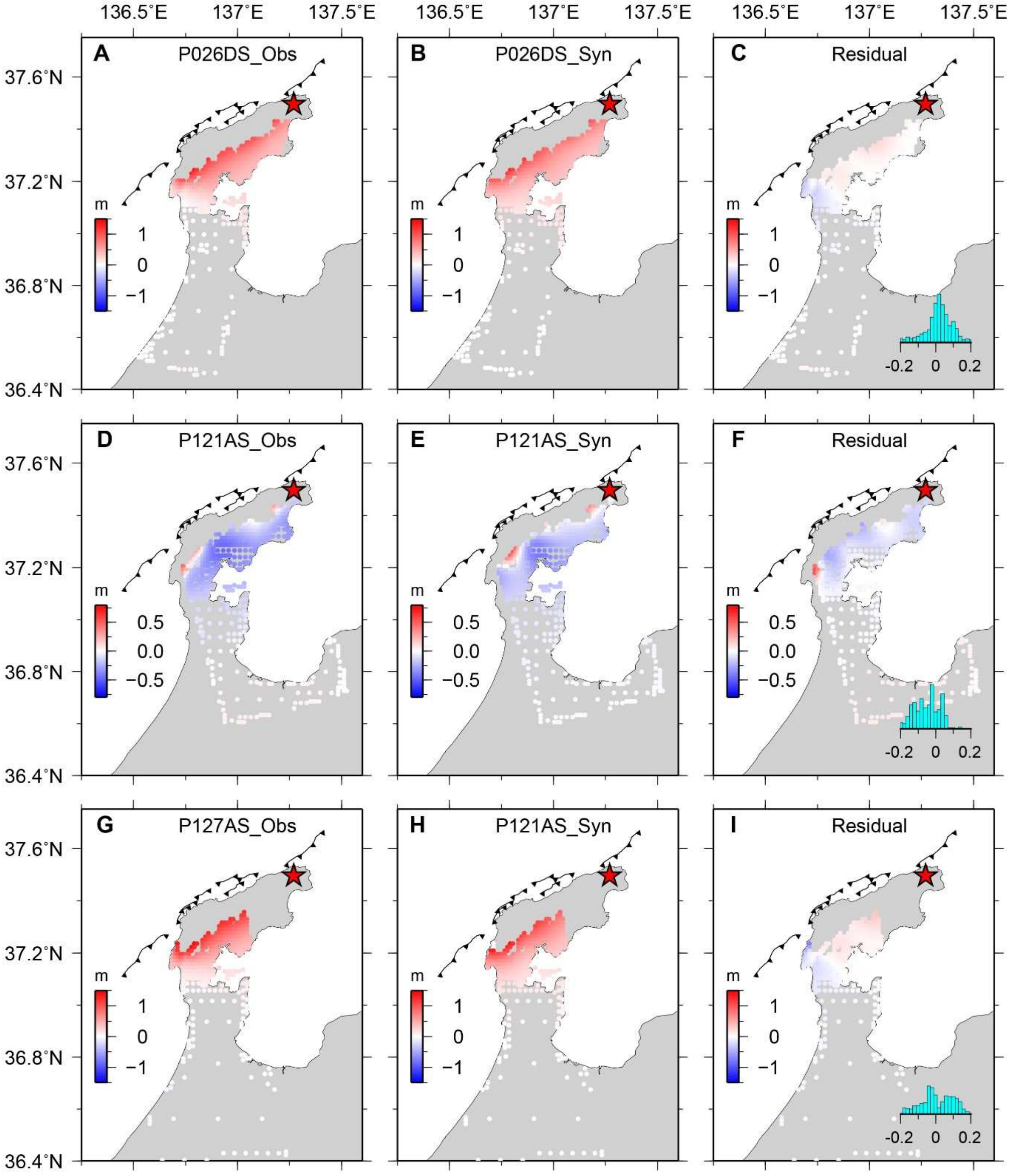

Fig. S16A. Fits to the InSAR LOS displacements for the preferred rupture model in Figure 6. (A), (D), and (G) show the LOS displacements of the descending track P026 and ascending tracks P121 and P127, respectively. (B), (E), and (H) indicate the corresponding predictions of range offsets derived from the preferred joint slip model. (C), (F), and (I) show residuals of range offsets along the ascending and descending paths, respectively. The active faults are denoted by black barbed lines, with the 2024 M_W 7.5 earthquake epicenter marked by a red star.

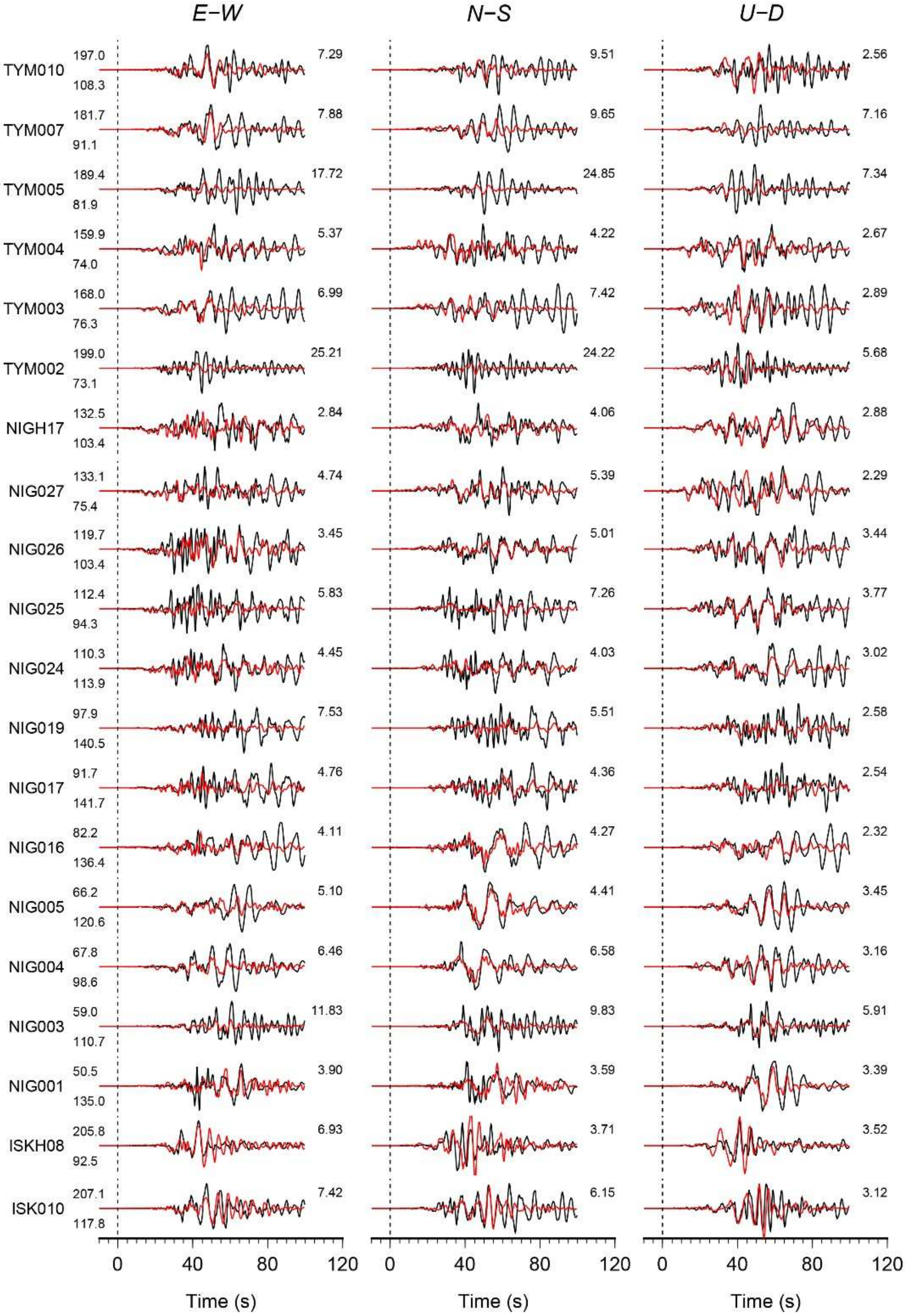

Fig. S16B. Comparisons of three-component strong-motion ground velocity observations (black) and synthetic seismograms (red) for the preferred joint model shown in Figure 6 and Figure S14A. Data and synthetics are aligned on the first *P* arrivals. The station name is listed on the left of each row. The azimuth (above) and epicentral distance (below) in degrees are shown at the beginning of each record. The numbers at the upper right of each waveform comparison indicate the maximum observed ground velocity in cm/s.

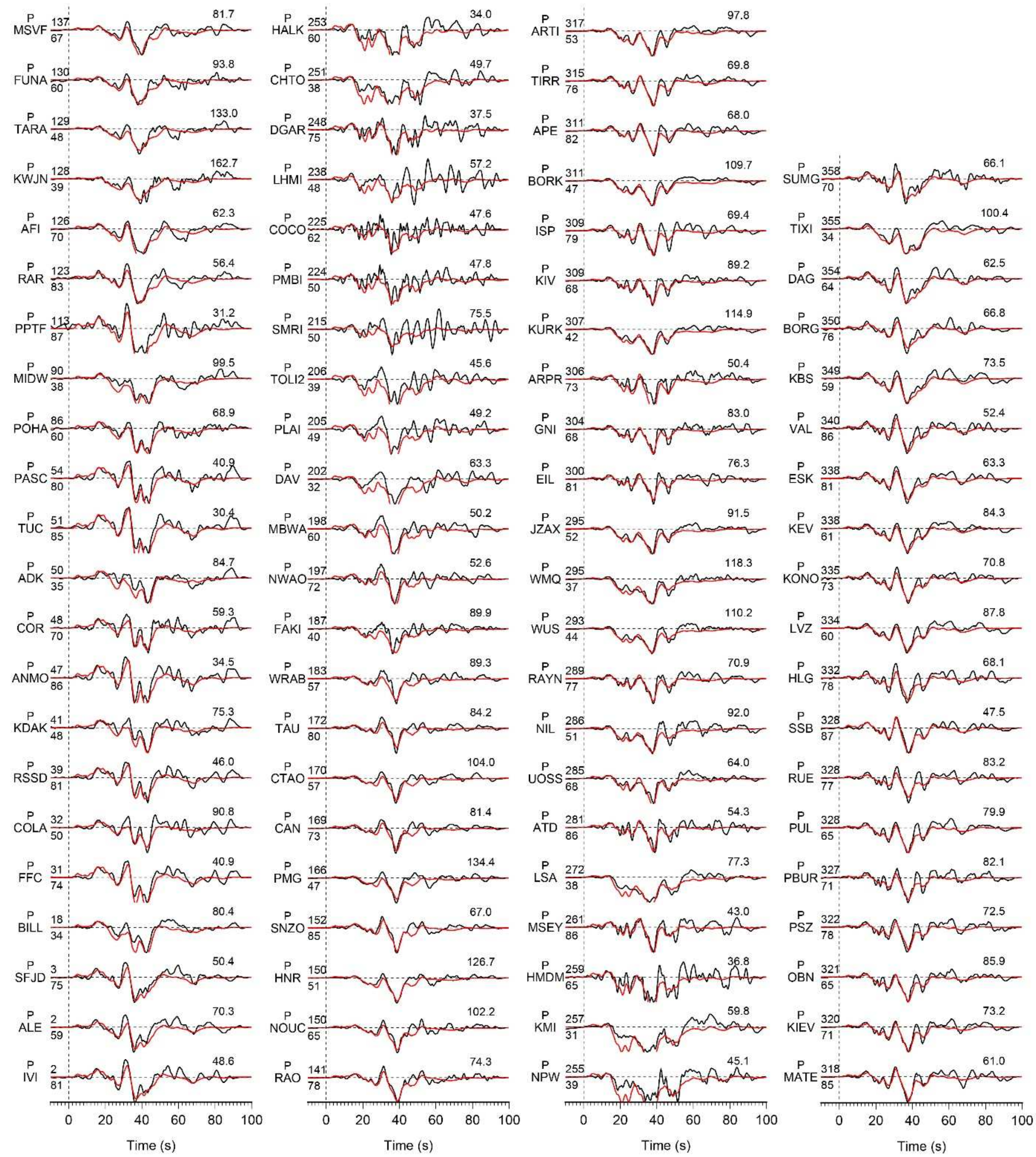

Fig. S16C. Comparison of observed (black) and synthetic (red) teleseismic *P*-wave ground displacements for the preferred model shown in Figure 6 and Figure S14A. Data and synthetic seismograms are manually aligned on the first arrivals. Station names and phase types are indicated on the left of each comparison. The azimuth (above) and epicentral distance (below) in degrees are shown at the beginning of each record. The number above the right portion of each comparison is the peak amplitude of the observed ground displacement in μm.

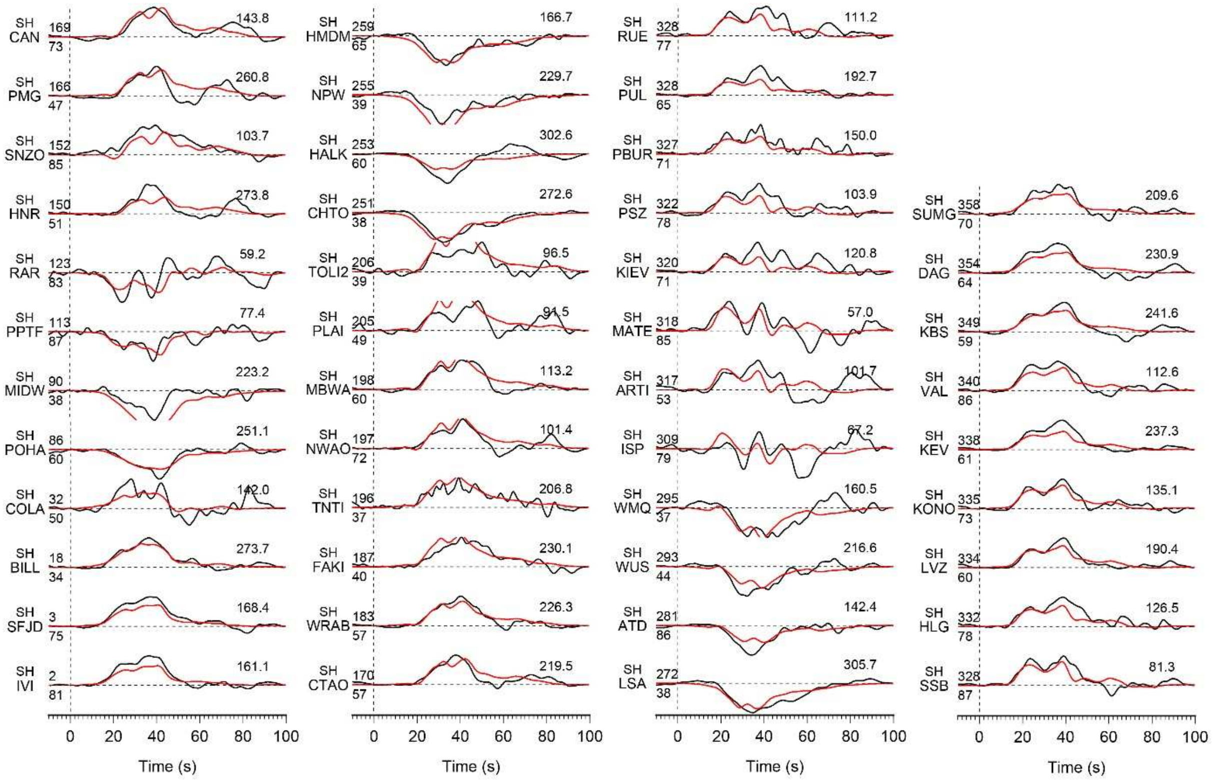

Fig. S16D. The same as Figure S16C, but for *SH*-waves.

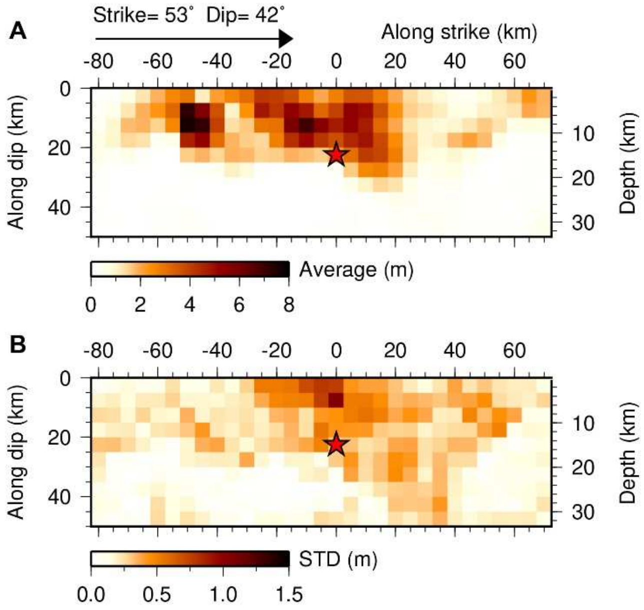

Fig. S17. The average slip distribution (A) and standard deviation (STD) estimates (B) of ten models with different random seeds for the 2024 M_W 7.5 earthquake.

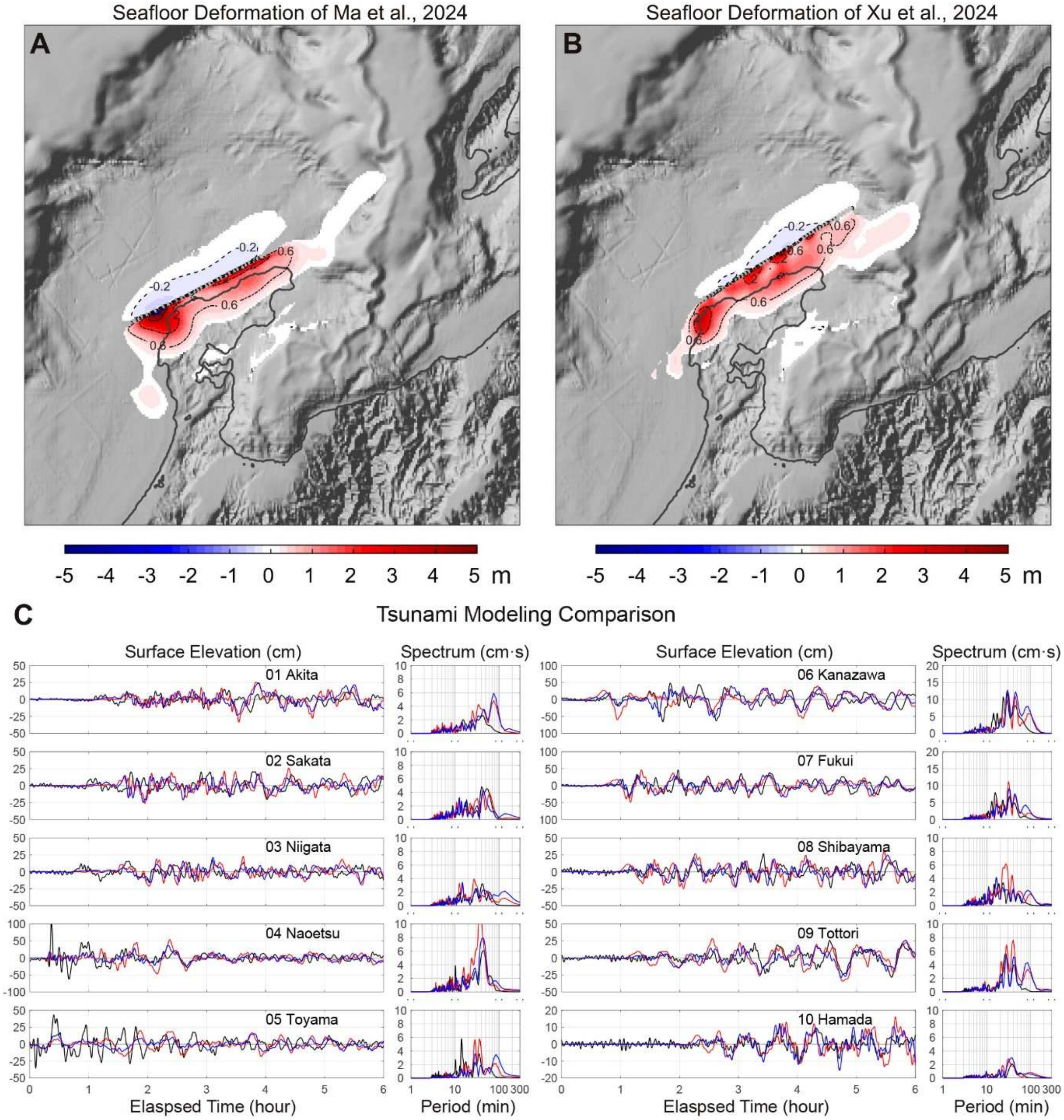

Fig. S18. Tsunami predictions for the slip models of Ma et al. (2024) (red lines) and Xu et al. (2024) (blue lines). (**A**) and (**B**),Vertical seafloor and land surface deformation computed for the models of Ma et al. (2024) and Xu et al. (2024), respectively. (**C**), Comparison of tsunami waveforms and predictions at the seafloor pressure stations shown in Figure 2A. Black lines represent observed time series (left) and amplitude spectra (right), while the predictions are indicated by colored lines.

Table S1. Dataset used for the 2024 M_W 7.5 and 2023 M_W 6.2 Japan earthquakes in this study.

Events	Satellite Sensor	Track*	Reference image	Secondary image	Temporal Baseline	Perpendicular Baseline	LOS		Range offset
							σ	α	σ
			yyyymmdd	yyyymmdd	days	m	cm	km	cm
20240101	ALOS-2 Stripmap	P121A	20220926	20240101	462	-141	15	41	14.3
		P127A	20231206	20240103	28	282	8.4	6.6	5.6
		P026D	20230606	20240102	210	124	13	34	9.5
20230505	Sentinel-1	T017D	20230504	20230516	12	18	4.2	62	-

*A and D indicate ascending and descending, respectively. For the LOS displacements, $\boldsymbol{\sigma}$ is the standard deviation calculated with all points in the nondeforming area, and $\boldsymbol{\alpha}$ is the e-folding correlation length scale of the 1D covariance function. For the range offset, the uncertainties are calculated using all points in the nondeforming area with a window of 100 × 100 pixels.

Table S2. Ranges of the source parameters allowed for each subfault during the joint inversion.

	The M_W 6.2 event	The M_W 7.5 event
Subfault size (km^2)	2.0×2.0	5.0×5.0
Slip (m)	(0.0, 5.0)	(0.0, 15.0)
Rake (°)	(39, 159)	(48, 168)
Rise time (s)	(0.4, 4)	(1.4, 14)
Velocity (km/s)	(0.25, 2.5)	(0.25, 2.25)